XIII. PLASMAS AND CONTROLLED NUCLEAR FUSION

A. Active Plasma Systems[*]

Academic and Research Staff

Prof. L. D. Smullin
Prof. A. Bers

Prof. R. J. Briggs
Prof. R. R. Parker

Graduate Students

R. R. Bartsch
S-L. Chou
G. W. Goddard

D. S. Guttman
F. Herba
B. R. Kusse
R. K. Linford

J. A. Mangano
J. A. Rome
H. M. Schneider

1. SYSTEM D: SPECTROSCOPIC MEASUREMENT OF THE ION TEMPERATURE

Introduction

The velocity distribution function of the ions in a plasma may be determined from the Doppler broadening of spectral lines radiated by the ions. In particular, if other broadening mechanisms are neglected, the shape of a spectral line radiated from ions in local thermodynamic equilibrium is given by the familiar Gaussian

$$I_D(\lambda) = \left(\frac{m_i c^2}{2\pi k T \lambda_o^2}\right)^{1/2} \exp\left[-\frac{m_i c^2}{2kT}\left(\frac{\lambda - \lambda_o}{\lambda_o}\right)\right]^2 , \tag{1}$$

where λ_o equals the radiated wavelength of the unbroadened line, and T is the ion temperature. The factor multiplying the exponential serves only to normalize the integral of the curve over wavelength to unity. The full width of the line at half-intensity characterizes the temperature of the radiating species. For a single spectral line this width, given by

$$w_D = 2\left(\frac{2kT \ln 2}{m_i c^2}\right)^{1/2} \lambda_o,$$

may be measured and the temperature computed. In practice, however, this simple procedure is complicated by three effects: the fine structure of a spectral "line"; the Zeeman effect, and other broadening mechanisms.

Theory

The series of spectral lines that were used in the temperature measurements described here are centered at 4685.75 Å and result from electronic transitions in the singly ionized helium atom. The fine structure of this series of lines has been studied extensively by Sommerfeld and Unsold,[1] who computed the relative intensities of each line in the series. The intensities and wavelengths of the five most intense lines in the series are given in Table XIII-1. The remaining fine-structure lines in this series have intensities less than 5 on the intensity scale established in Table XIII-1 and were neglected. If the Doppler effect were the only broadening mechanism present, the resultant shape of the He II 4685.75 series of lines could be determined by centering Gaussian curves of the form given by Eq. 1 at the wavelengths and with the amplitudes prescribed by Table XIII-1. A superposition of these curves would then give the resultant relative amplitude for each wavelength.

Table XIII-1. Wavelengths and intensities of the five most intense lines in the series.

λ (Å)	Relative Intensity (as calculated by Sommerfeld and Unsold)
4685.378	19.5
4685.408	10.3
4685.569	5.1
4685.705	100.0
4685.805	92.3

The Zeeman effect results in the splitting of each of the fine-structure lines, because of an applied magnetic field. In accounting for this effect, we have considered only the normal Zeeman splitting. This classical theory[2] predicts that each fine-structure line will be split into three lines (classical triplet): one line (π line) remains at the original wavelength, while the two other lines (σ lines) are displaced in wavelength equally above and below the central line by an amount that is proportional to the magnetic field. When viewed across the magnetic field, the relative amplitude of the π line is twice that of the σ lines if the states are equally excited. Since its electric field is polarized along the magnetic field, the π line is invisible when the plasma is viewed along the magnetic field. The field of the σ lines is circularly polarized in a plane perpendicular to the magnetic field, and thus the σ lines are always visible. Therefore the 5 original fine-structure lines are split into 15 lines when the plasma is viewed transversely (to the

magnetic field) and into 10 lines when the plasma is viewed longitudinally.

A consideration of line-broadening mechanisms other than thermal Doppler broadening is essential for laboratory plasmas. Of these mechanisms the Stark effect and nonthermal Doppler broadening are usually most important. Stark broadening, the dominant subclass of pressure broadening in our plasma, is an electric field effect and has been studied extensively by Griem and his co-workers.[3] The magnitude of this effect for the He II 4685.75 series can be determined from an extrapolation of the atomic Stark coefficients, $C(n_e, T_e)$, computed by Griem.[3] Using this coefficient, which is a weak function of the electron density and temperature, in Eq. 2 gives us the full width at half-intensity of a Stark-broadened line.

$$w_s = \left[\frac{n_e}{C(n_e, T_e)} \right]^{2/3} \tag{2}$$

Assuming a plasma density of 5×10^{12} electrons/cm^3 and an electron temperature of 10 eV, we find that $w_s = 0.03$ Å. At densities typical of our discharge, then, Stark broadening is much smaller than the expected Doppler broadening, and thus is neglected in our computations of the ion temperature. We must point out that Griem's calculation of $C(n_e, T_e)$ does not include the effects of turbulent microelectric fields, which are thought to be associated with the beam-plasma discharge.[4] These effects could conceivably increase the half-width computed from Eq. 2 measurably. The absence of the characteristic Lorentzian broadening in the far wings of our experimental curves indicates, however, that this anomalous Stark effect is small. Therefore these effects have been neglected.

Nonthermal Doppler broadening of the spectral lines is caused by macroscopic ion drifts in the plasma. When a plasma column is viewed transversely through its center, only the radial drift component Doppler-broadens the emitted spectral lines. Radial drifts, however, are retarded by the confining nature of the magnetic field and thus are negligible. When the plasma is viewed longitudinally, only axial drifts contribute to the nonthermal Doppler broadening. Ion drifts caused by potential gradients in the plasma can be significant,[5] and may lead to large nonthermal Doppler broadening. These drifts are, at present, under study, but, in this report, were not included in the determination of the parallel ion temperature.

In summary, the effects included in the calculation of a theoretical line shape for the He II 4658.75 series are (i) thermal Doppler broadening, (ii) fine structure, and (iii) normal Zeeman splitting. All other broadening mechanisms were assumed to be negligible for the reason stated. The experimental validity of this assumption will be appreciated later.

A computer was used to superpose Gaussian curves of the proper relative amplitudes
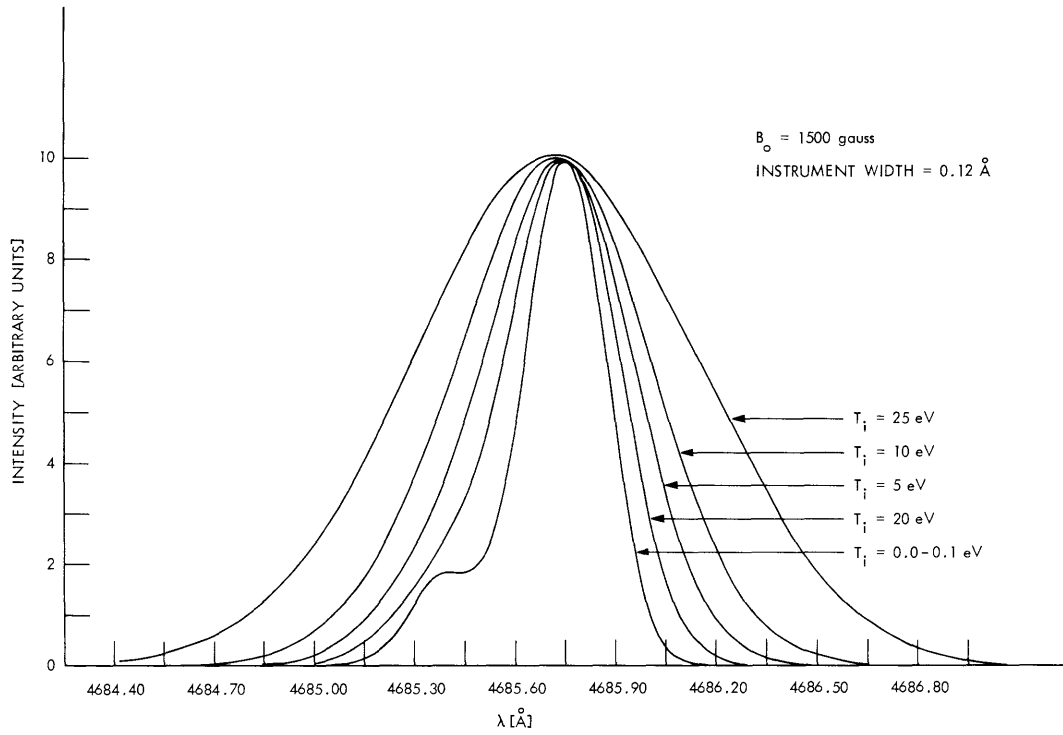
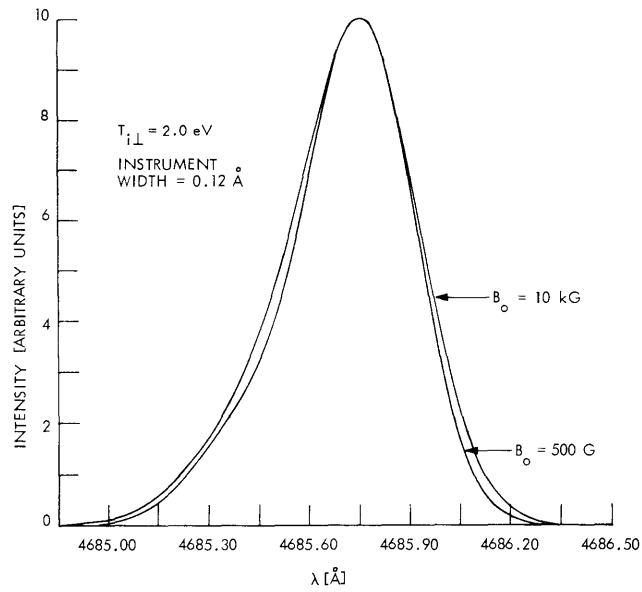Fig. XIII-1. Line shape as a function of ion temperature.

Fig. XIII-2. Line shape as a function of magnetic field.

centered at wavelengths dictated by fine-structure and Zeeman-splitting effects. The width of each Gaussian is given by

$$w = \left[w_D^2 + w_I^2 \right]^{1/2},$$

where w_I is the full half-width of a single unbroadened spectral line as viewed through the experimental apparatus. Since the instrument function is nearly Gaussian, the square of the half-widths may be added as shown. Figure XIII-1 shows examples of the resulting computer curves at several ion temperatures for the He II 4685.75 series viewed transversely. Here we have used a magnetic field of 1500 G and an instrument width, w_I, of 0.12 A. Figure XIII-2 shows the weak dependence of these curves on magnetic field at a constant ion temperature of 2 eV, and an instrument width of 0.12 A. The magnetic fields used in our experiments vary from 500 G to 10 kG. Hence in these experiments the Zeeman effect is small but not negligible at the higher magnetic fields.

Experiment

The experimental apparatus used to measure the He II 4685.75 line shape is shown in Fig. XIII-3. Light from the plasma was condensed with a lens (f=9.6 cm) focussed on
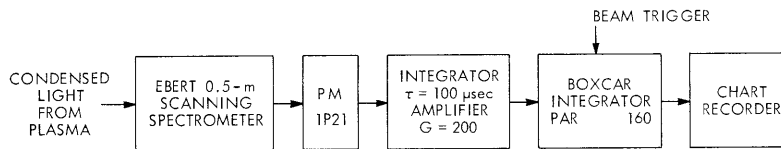

Fig. XIII-3. Experimental apparatus.

the entrance slit of a 0.5-m Ebert scanning spectrometer (Jarrell-Ash Company Model 82-000). The straight, variable entrance and exit slits of the spectrometer were 14 μ wide and 2 mm high. (The instrument half width with these slit dimensions was found to be .12 A, using the Hg I 5460.74 line from a Geissler tube as a calibration source. The self-broadening of this line is known to be negligible compared with the measured instrument broadening.) The light passed through the spectrometer to a magnetically shielded photomultiplier tube (RCA 1P21). The resulting PM tube signal was integrated for 100 μsec and amplified. Since the beam-plasma discharge was created for 660 μsec once every 2 sec, it was necessary to average over many plasma pulses. Consequently, the spectrometer was scanned very slowly $\left(\frac{1}{25} \; \overset{\circ}{A}/min \right)$ with a geared-down, 1 rpm synchronous motor. The pulsed output of the amplifier was sampled for 20 μsec at a fixed time interval after the start of the beam pulse by a boxcar integrator (PAR Model CW-1).
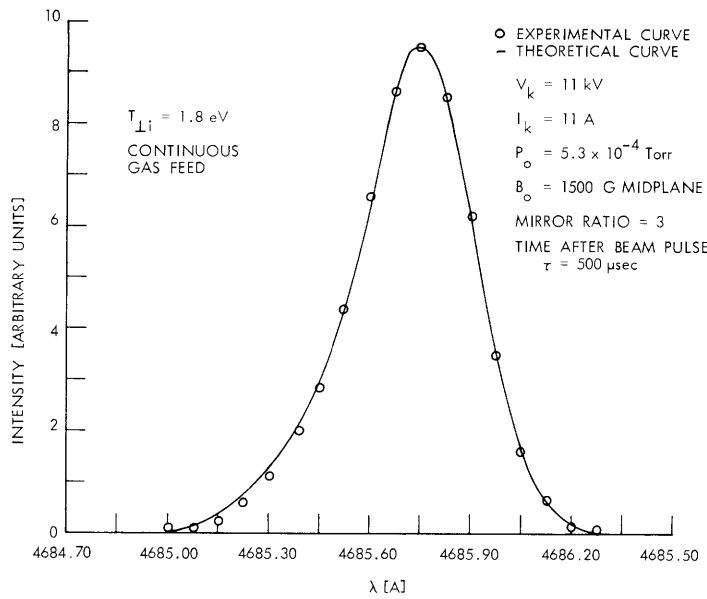
○ EXPERIMENTAL CURVE
— THEORETICAL CURVE

$V_k = 11$ kV

$I_k = 11$ A

$P_o = 5.3 \times 10^{-4}$ Torr

$B_o = 1500$ G MIDPLANE

MIRROR RATIO = 3

TIME AFTER BEAM PULSE
$\tau = 500$ μsec

$T_{\perp i} = 1.8$ eV
CONTINUOUS
GAS FEED

Fig. XIII-4.

Typical line shape: continuous gas feed looking transversely.

○ EXPERIMENTAL CURVE
— THEORETICAL CURVE

$V_k = $ kV

$I_k = 8$ A

$P_o = 5.3 \times 10^{-4}$ Torr

$B_o = 1500$ G MIDPLANE

MIRROR RATIO = 3

TIME AFTER BEAM PULSE
$\tau = 500$ μsec

$T_{\parallel i} = 1.7$ eV
CONTINUOUS
GAS FEED
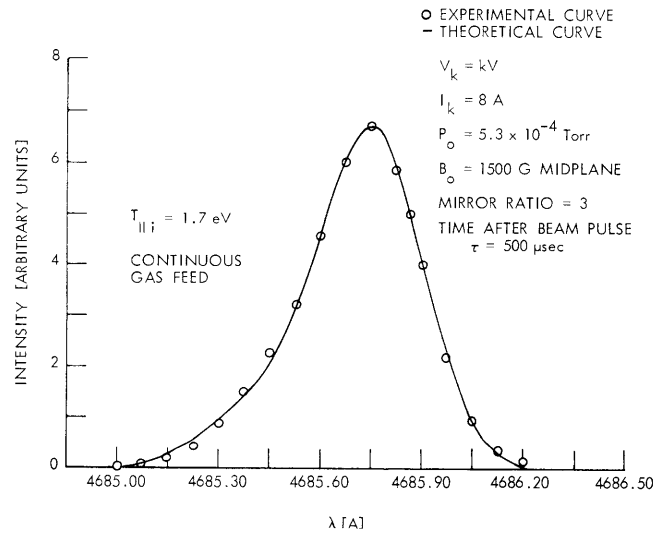
Fig. XIII-5.

Typical line shape: continuous gas feed looking longitudinally.

○ EXPERIMENTAL CURVE
— THEORETICAL CURVE

$V_k = 8.5$ kV

$I_k = 10$ A

$P_{o\ peak} = 3 \times 10^{-5}$ Torr

$B_o = 500$ G MID-PLANE

TIME AFTER BEAM PULSE
$\tau = 500$ μsec

$T_{\perp i} = 5.4$ eV
PULSED GAS FEED
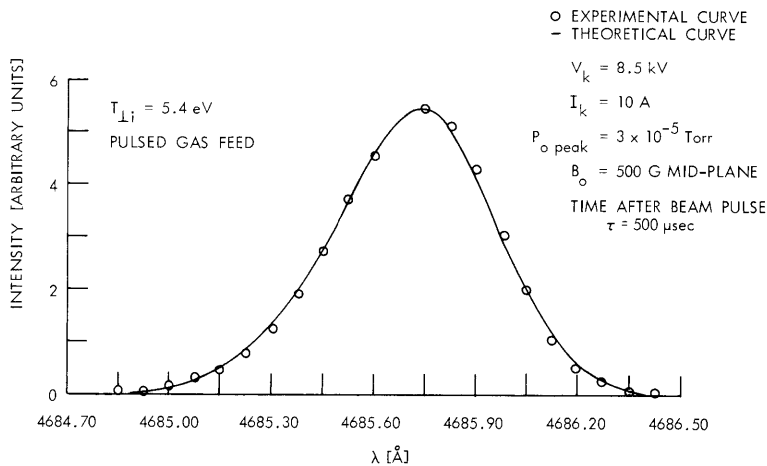
Fig. XIII-6.

Typical line shape: pulsed gas feed looking transversely.

These samples were then averaged by the boxcar and the resulting average of many pulses was continuously recorded on a chart recorder. The resulting curve represents the line shape for a given 100 μsec during the beam pulse, averaged over many beam pulses.

Preliminary Results

Computer-generated He II 4685.75 line shapes were fitted to the experimental curve to determine the ion temperature. The magnetic field, the instrument broadening, and a given ion temperature serve to determine the shape of the computer curves. Since the magnetic field and instrument broadening were known, the ion temperature was the only parameter varied in the best-fit procedure, except for an amplitude factor. Results of the best-fit procedure are shown for 3 experimental curves in Fig. XIII-4, XIII-5 and XIII-6. The solid line in these figures is the computer-generated curve, while the circles indicate the shape of the experimental curve. These figures show typical curves for continuous gas feed looking transversely (Fig. XIII-4), continuous gas feed looking longitudinally (Fig. XIII-5), and pulsed gas feed looking transversely (Fig. XIII-6). The ion temperature reported for the pulsed gas feed measurement may not be typical of optimum pulsed gas operation. The beam collector position for our measurement was wholly outside the magnetic bottle region. The most intense discharge has been reported when this collector is placed partially within the bottle region.[6]

At the present time, the position of the pulsed gas feed precludes our looking longitudinally in this gas feed mode. The curves show typical ion temperatures, together with the beam-plasma operating conditions under which the experimental curves were made. The accuracy of the ion temperature measurements reported here is estimated to be ±0.2 eV.

J. A. Mangano, L. D. Smullin

References

1. A. Sommerfeld and A. Unsold, Z. Physik 38, 237 (1926).

2. H. E. White, Introduction to Atomic Spectra (McGraw-Hill Publishing Company, New York, 1934), Chap. 10.

3. H. R. Griem, Plasma Spectroscopy (McGraw-Hill Book Company, New York, 1964).

4. E. V. Lifshitz, et al., "Spectroscopic Study of the Interaction of Charged-Particle Beams with Plasmas," Soviet Physics — Tech. Phys. 11, 798 (1966).

5. D. A. Dunn and S. A. Self, "Static Theory of Density and Potential Distribution in a Beam-Generated Plasma," Technical Report No. 0311-1, Stanford Electronics Laboratory, July 1963.

6. L. D. Smullin, "Recent Results on the Beam-Plasma-Discharge: A Survey of Phenomena in Ionized Gases," invited papers, International Atomic Energy Agency, Vienna, 1968.

2. HEXAPOLE EXPERIMENT

Since our last report we have performed spectrum measurements of the signal detected by an electrostatic probe inserted into the plasma. The probe was placed approximately 4 cm away from the axis of the system at the edge of the plasma column. The probe was terminated in 50 Ω and the resultant signal was analyzed by first mixing it with a local oscillator of frequency 1.6 MHz and then passing the output into a Tektronix 1L10 spectrum analyzer, used as a tunable receiver. The receiver frequency was swept slowly, and the output was averaged by means of a PAR boxcar integrator and recorded on a chart recorder.

Results of runs taken at different magnetic fields and constant pressure and beam conditions are shown in Fig. XIII-7. In each case, the large spike occurring at zero frequency is due to unbalance in the mixer and is effectively a zero-frequency marker. The other spikes are due to unstable plasma modes whose structure is clearly dependent on the magnetic field. We tentatively identify these modes as the rotating flutes investigated in detail by Hartenbaum
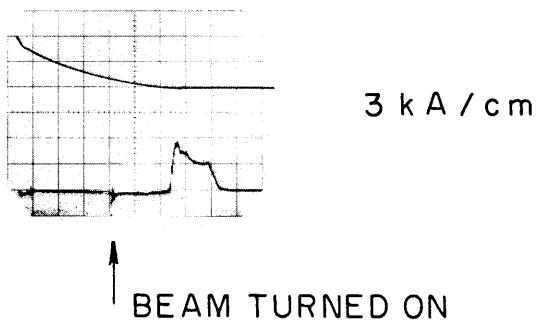
Fig. XIII-7. Spectrum measurements of probe signal as a function of the mirror field B_o.

Fig. XIII-8.
Upper trace: Hexapole current. Lower trace: Probe signal. Horizontal axis: 50 µsec/cm.
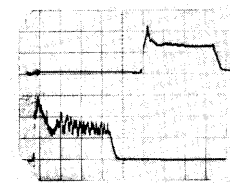
3 k A / c m

BEAM TURNED ON
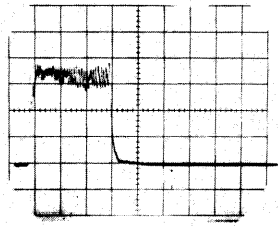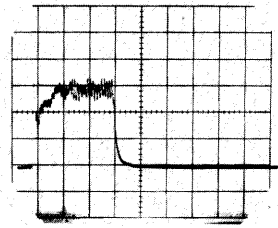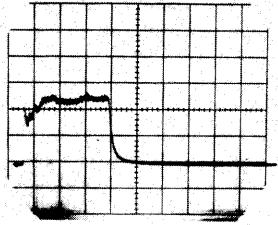
Fig. XIII-9.
Probe signals with (upper) and without (lower) hexapole field. Upper trace shows a delay of 250 µsec in the beam pulse with respect to the hexapole.
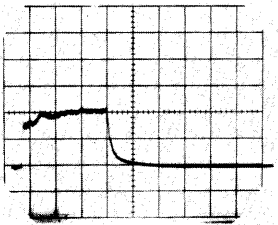
$I_H = 0 A$

$I_H = 80 A$

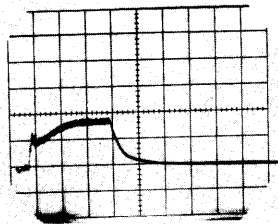$I_H = 100 A$

$I_H = 140 A$

$I_H = 200 A$

$50 \mu \, sec/cm$

Fig. XIII-10. Probe signal as a function of the hexapole current I_H.
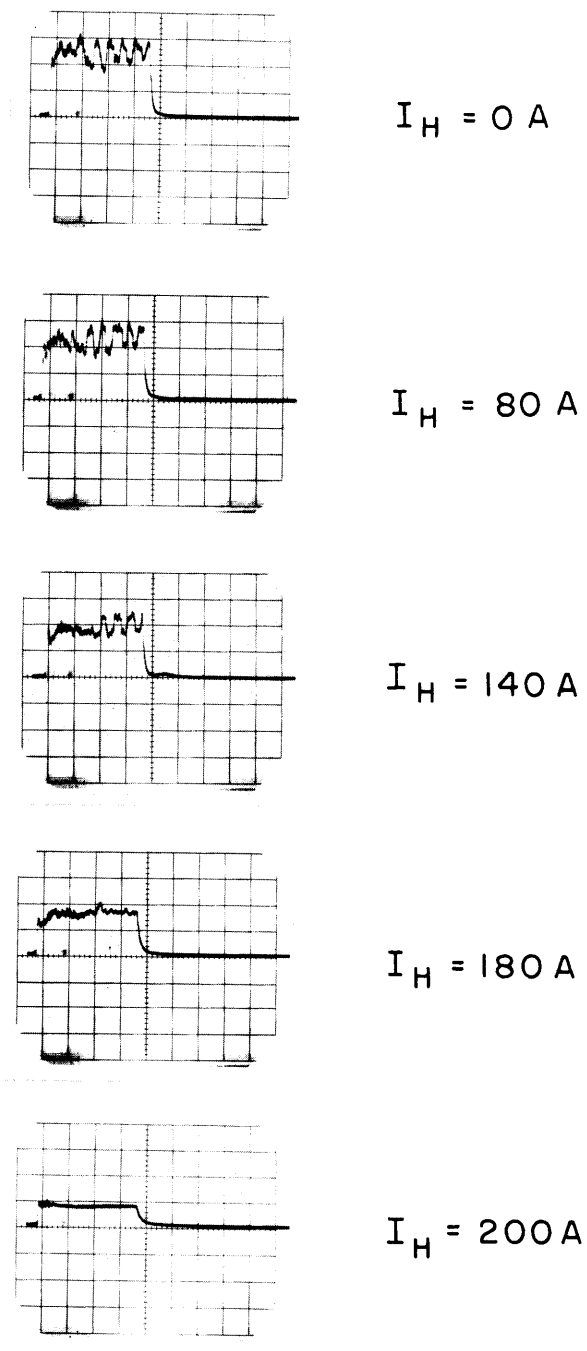Mirror field 100 G; pressure 1.4×10^{-3} Torr.

$I_H = 0\ A$

$I_H = 80\ A$

$I_H = 140\ A$

$I_H = 180\ A$

$I_H = 200\ A$

Fig. XIII-11. Probe signal as a function of the hexapole current I_H.
Mirror field 170 G; pressure 1.26×10^{-3} Torr.

in a similar experiment.[1]

As we discussed previously, the pulsed hexapole system is now operational. A major difficulty has been encountered in its use, however. We have found that, regardless of the time at which the beam is fired relative to the start of the hexapole-current pulse, a discharge does not take place <u>until</u> the hexapole current has decayed to an extremely small value. This effect is illustrated in Fig. XIII-8, which shows the hexapole-current pulse and the signal detected by the probe. The beam was fired at the time indicated, and it is seen that the plasma does not form until the hexapole current has decayed to a small value.

We have attributed this effect to the electric field associated with the decaying magnetic field of the hexapole. To test this hypothesis, we passed a constant current of 200 A through the hexapole. This current is considerably less than that in the hexapole at the beginning of the current pulse, but much <u>greater</u> than the residual current in the hexapole when a discharge could occur. Under these conditions, the discharge forms regularly at the beginning of the beam pulse, just as in the case with no current in the hexapole.

In spite of the difficulties with the pulsed field noted above, a remarkable effect has been observed; when the beam was fired very late with respect to the current pulse, the residual current in the hexapole, which amounted to approximately 20 A, was often sufficient to at least partially stabilize the resultant plasma. This effect is illustrated in Fig. XIII-9, where the probe signal with and without the hexapole current is shown. Thus, we have demonstrated that under certain conditions, only very weak hexapole fields are required to provide stabilization.

Having observed this effect, we have begun investigation of the stabilizing effects of the hexapole when excited by direct current. While the maximum DC current available (200 A) is much less than that obtainable from the pulsed system, it is still sufficient to stabilize the plasma under a wide range of conditions. This is illustrated in Figs. XIII-10 and XIII-11, which show the probe signal with hexapole current as a parameter, for two values of the midplane magnetic field. In both cases, the plasma decay time is seen to increase and the average probe signal has decreased, thereby suggesting a decrease in the size of the column. A more detailed, parametric study of these effects is under way.

F. Herba, R. R. Parker

References

1. B. Hartenbaum, "Experimental Investigation of the Beam-Plasma Discharge," Ph. D. Thesis, Department of Mechanical Engineering, M. I. T., May 1964.

3. INTERACTIONS OF A SPIRALING ELECTRON BEAM WITH A PLASMA

The spiraling electron beam-plasma experiment has been described in previous reports.[1,2] A hollow, cylindrical electron beam is formed and injected through a sharp magnetic cusp. The cusp magnetic field causes the beam to rotate about its axis. The spiraling beam then flows through a background gas in an interaction region enclosed by a screen conducting cylinder as shown in Fig. XIII-12. A uniform axial magnetic field exists in this interaction region.

This report discusses some of the recent experimental observations of the instability which results when the spiraling beam interacts with the plasma it produces. Some of the properties of this instability have been discussed previously.[2,3] The data presented in this report were taken when various modes of the instability were present.

Density Measurements

Plasma density measurements have been made using a Langmuir probe. The plasma densities were low and ranged between 10^8 and 10^9 per cubic centimeter. Even with a spherical probe, 0.475 cm in diameter, the Debye length was larger than the probe dimension, and consequently conventional ion saturation currents could not be seen.

A computer study of Langmuir probes whose dimensions are comparable to and smaller than a Debye length has been made by J. G. Laframboise.[4] Using curve-fitting techniques and the results given by Laframboise, we were able to analyze our probe curves for plasma density.

The Langmuir probe used in making the density measurements is shown in Figs. XIII-12 and XIII-13. The collecting surface was a 0.475 cm K-Monel ball mounted on an L-shaped rod, the rod being insulated from the plasma particles. By sliding the rod, the probe could be moved axially along the system. By rotating the rod to different ϕ-positions (see Fig. XIII-13) the collecting sphere could be moved from a position on the system axis to one outside the shell of the beam, thereby yielding density information as a function of radius. In making the radial profile measurements, the sphere was rotated through the beam. To a large extent, the density of the plasma is a function of the probe electron current at a given voltage, the higher the current the higher the density. Therefore when the sphere was in such a position that the beam electrons could strike it, secondary electrons could leave the probe surface; this could very well have caused a reduction of the total probe electron current. No attempt has been made to compensate for these secondary electrons in the analysis of the probe curve. Consequently, the values of plasma density for positions in the area of the beam are probably low.
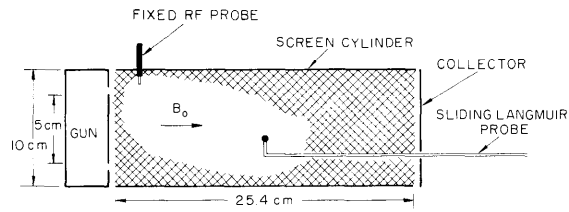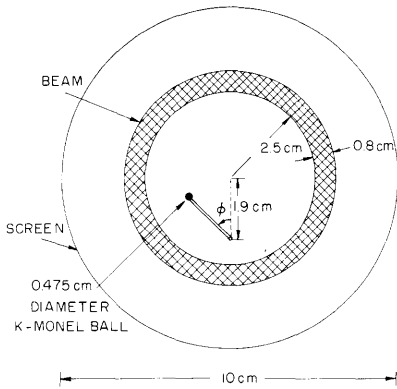
Fig. XIII-12. Interaction region.

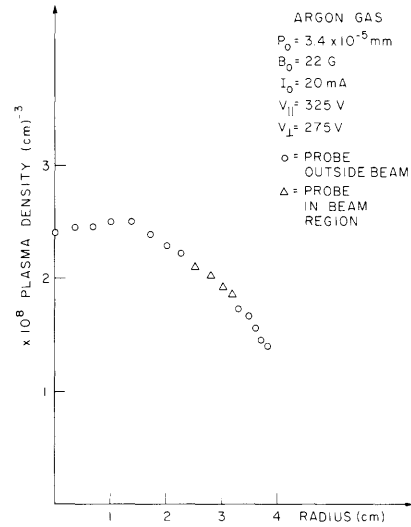Fig. XIII-13. Movable Langmuir probe.
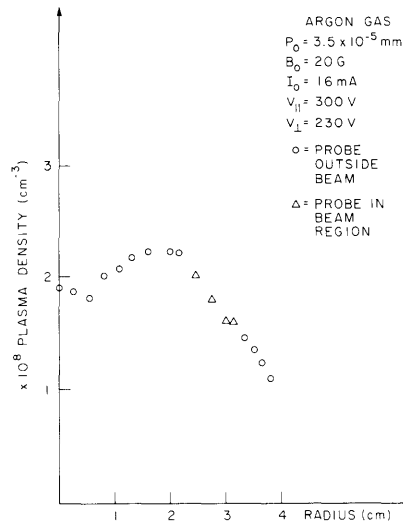

Fig. XIII-14. Radial density profile I.

Fig. XIII-15. Radial density profile II.

As mentioned, profiles were taken during various modes of the instability. Very little axial variation of the density was observed. Within 1-2 cm of the ends of the interaction region the density dropped rapidly. In the remaining region the density appeared constant within approximately 15%. Radially, however, two general types of profiles were observed and are shown in Figs. XIII-14 and XIII-15. The experimental conditions are given in the upper right-hand corners of the figures. B_o is the axial magnetic field in the interaction region; P_o, the background gas pressure in mm Hg as measured by an R. L. E. ionization gauge; I_o, the total DC beam current, and $V_\parallel$ and $V_\perp$, the beam energy along and across the magnetic field. The main difference between these two profiles is that the density in Fig. XIII-14 is relatively uniform in the region between the beam and the axis, while it drops slightly over the same region in Fig. XIII-15. The plasma electron temperature was obtained in the conventional manner from the exponential region of the Langmuir probe curves. The plasma electron temperature for the conditions of Fig. XIII-14 was approximately 11 V, while the temperature for the conditions of Fig. XIII-15 was approximately 5 V. Therefore, the plasma which existed under the conditions of Fig. XIII-14 could diffuse more easily across the magnetic field.

These two density profiles are typical of the experimental results. Either the density was relatively uniform in the central region, or it dropped slightly on the axis. Between the beam and the screen the density dropped rapidly. The probe allowed measurements within approximately 1 cm of the screen.

Measurements of the RF Oscillations

During the beam-plasma instability which has been observed in the experiment, narrow-band RF oscillations have been seen.[2,3] These oscillations occur in a range of frequencies between 30 MHz and 150 MHz. To study these oscillations, the ball at the end of the sliding Langmuir probe was replaced by an antenna approximately 0.5 cm long. The antenna was oriented axially and the signal fed to a detector by a shielded cable through an L-shaped glass rod as shown in Fig. XIII-16. With this probe measurements of the RF signal could be made as a function of axial and radial position. Rotating this probe in ϕ also allowed investigation of the signal as a function of θ, the angle taking as its axis the system axis (see Fig. XIII-16). The fixed RF probe shown in Fig. XIII-12 was used as a reference probe for the following measurements.

a. Quenching

While the experiment was running continuously the RF oscillations observed during the interaction were amplitude-modulated. An example of this amplitude modulation,
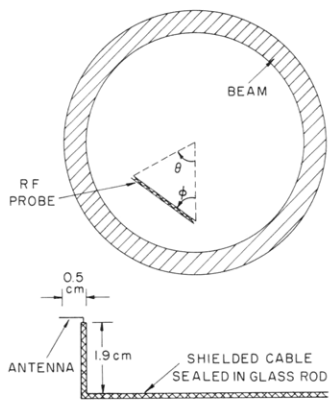
Fig. XIII-16. Movable RF probe.
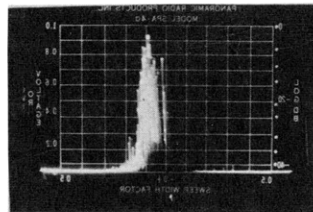
CENTER FREQUENCY 37 mHz

I mHz / 4 DIVISIONS

Fig. XIII-17.
Quenching and
frequency spread.

5 μ sec / cm

ARGON GAS

$P_o = 3.4 \times 10^{-5}$ mm $V_{\parallel} = 30$ V

$B_o = 10$ G $V_{\perp} = 120$ V

$I_a = 0.75$ mA

ARGON GAS
$P_o = 3.4 \times 10^{-5}$ mm
$B_o = 13$ G
$I_o = 50$ mA
$V_{\parallel} = 132$ V
$V_{\perp} = 96$ V

o = PROBE OUTSIDE BEAM
$\triangle$ = PROBE INBEAM REGION
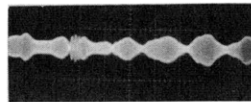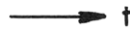
Fig. XIII-18. Radial RF Profile.

Fig. XIII-19. Wavelength analyzer.

Fig. XIII-20. Axial wavelength.
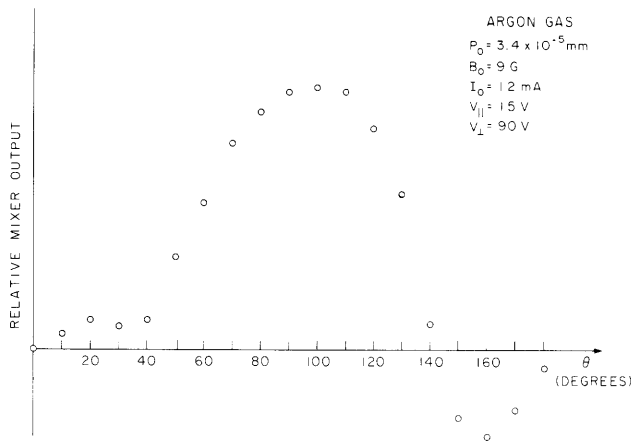
Fig. XIII-21.

Azimuthal wavelength, m = 1.

Fig. XIII-22.

Azimuthal wavelength, m = 2.

or quenching, is shown in Fig. XIII-17. The experimental conditions are shown. The upper trace is a picture of the spectrum analyzer. The lower one is a picture of the signal as observed on a Tektronix 585 oscilloscope. It can be seen that the modulation could very well account for the spread in frequency observed on the spectrum analyzer. The per cent and frequency of the modulation varied with experimental conditions.

b. Radial RF Profile

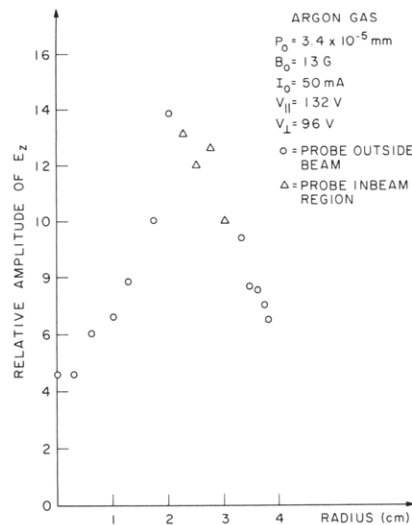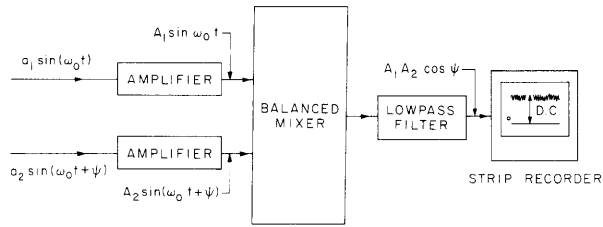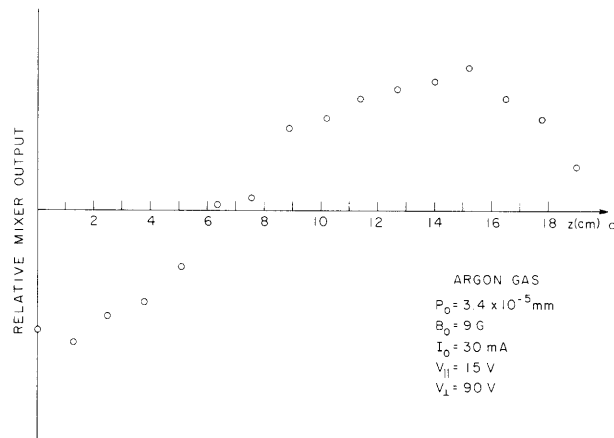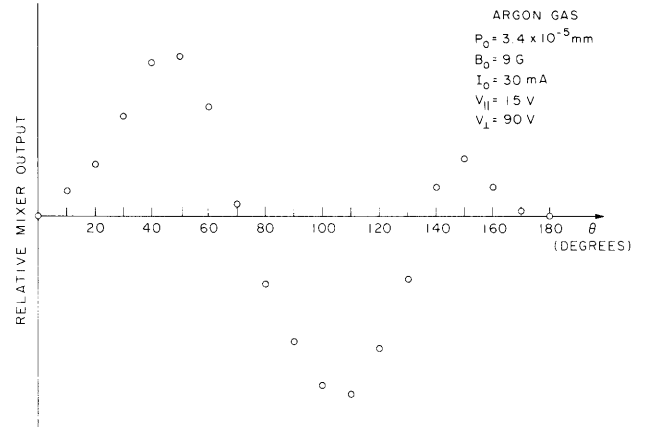By rotating the sliding RF probe, radial profile data were taken. As the movable probe was adjusted to different radial positions, the signal on the fixed RF probe was monitored. The amplitude from the movable probe was divided by the amplitude on the fixed probe. This relative amplitude as a function of radial position is shown in Fig. XIII-18. Typically the field was maximum in the region of the beam and dropped off as the probe was moved away.

c. Wavelength Measurements

The measurement of spatial wavelengths requires comparison of signals taken from two different positions. When the signal under observation is an unstable oscillation of a system it is crucial that the measuring device not couple the signal from one position to the other. Various methods were attempted, and we finally used a technique similar to the one described by Bousquet and his co-workers.[5]

Signals from the two RF probes in our experiment were fed into amplifiers and then to the two input ports of a balanced mixer (see Fig. XIII-19). The two input ports were isolated by approximately 25 db. These signals were of the same frequency but of different time phase ψ (see Fig. XIII-19). The DC output of the mixer was then recorded on a strip chart recorder, the displacement of the recorder being proportional to the cosine of the phase difference between the two input signals. The strip chart was used to average the DC signal for approximately 3 sec for each position of the movable probe. The amplitudes of the signals at the outputs of the amplifiers were monitored. The DC output of the mixer was divided by their product. This normalized DC signal will be referred to as the relative mixer output. As the position of the movable probe was adjusted any variation in the relative mixer output was due only to the change in ψ. Standing-wave or convective variations of the signals would be removed by this normalization procedure. By using a line stretcher to reproduce the phase shift caused by moving the sliding probe, the direction of propagation was also determined.

Figure XIII-20 shows a typical result as the sliding probe was moved along the direction of the axis of the system. The position z = 0 is at the collector. The antenna was positioned about half way between the system axis and the beam. It can be seen

from Fig. XIII-20 that the phase variation is not exactly uniform with z. One can, however, associate ψ with kz and obtain an axial wavelength of approximately 25 cm. Checking the direction of propagation showed that it was in the direction of beam flow. Other observations have shown axial wavelengths as short as 10 cm.

With the sliding probe at a fixed position along the axis, rotating it through 360° in ϕ sampled the wave through 180° in θ. The results of such measurements are shown in Figs. XIII-21 and XIII-22. In these cases if ψ is associated with $m\theta$, Fig. XIII-21 is predominantly an $m = 1$ mode, while Fig. XIII-22 appears to be predominantly an $m = 2$ mode. In both of these cases evidence of lower amplitude, higher order modes can be seen. After checking the direction of propagation it was again observed that the waves were propagating azimuthally in the direction of beam rotation.

From these measurements it has been possible to find a correlation between the wavelength and the frequency of the RF oscillations. The frequency is apparently the Doppler-shifted frequency given by $m\omega_{ce} + kv_z$, where ω_{ce} is the electron-cyclotron frequency, and v_z is the beam velocity along the magnetic field.

Current Work

At present, we are in the process of extending a theoretical analysis based on a rigid-beam assumption.[3] Various ways of modeling the plasma and geometry are being investigated.

B. R. Kusse

References

1. B. Kusse and A. Bers, "Cross-Field Beam-Plasma Interactions," Quarterly Progress Report No. 82, Research Laboratory of Electronics, M. I. T., July 15, 1966, pp. 154-157.

2. B. Kusse and A. Bers, "Interaction of a Spiraling Electron Beam with a Plasma," Quarterly Progress Report No. 86, Research Laboratory of Electronics, M. I. T., July 15, 1967, pp. 154-156.

3. B. Kusse and A. Bers, "Spiraling Beam-Plasma Interactions," Quarterly Progress Report No. 88, Research Laboratory of Electronics, M. I. T., January 15, 1968, pp. 175-182.

4. J. G. Laframboise, "Theory of Spherical and Cylindrical Langmuir Probes in a Collisionless, Maxwellian Plasma at Rest," UTIAS Report No. 100, University of Toronto, Toronto, Canada, June 1966.

5. J. C. Bousquet, M. Parisot, F. Perceval, and M. Perulli, "Measurements of the Wave Length and Spectrum of Wave Numbers Associated with a Beam-Plasma System," EUR CEA FC 444 Report, October 1967.

4. OSCILLATIONS IN AN INHOMOGENEOUS COLD PLASMA

General Results for Asymptotic Response

The response of a one-dimensional, cold inhomogeneous plasma to an initial displacement perturbation δ is[1]

$$E(x, t) = \frac{e\delta}{\epsilon_0} n_0(x) \cos [\omega_p(x)t], \tag{1}$$

where E is the electric field, e the charge on an electron, and $n_0(x)$ the unperturbed electron number density. The quantity $\omega_p(x)$ is the local plasma frequency.

In this report we present some general results on the asymptotic time dependence of the voltage across the plasma, which is given by

$$V(t) = - \frac{e\delta}{\epsilon_0} \int_{-\infty}^{\infty} n_0(x) \cos [\omega_p(x)t] \, dx. \tag{2}$$

As t becomes large, the integral in equation (2) may be evaluated approximately by the method of stationary phase. This method is based on the fact that the major contribution to the integral as $t \to \infty$ comes from the points where the "phase" $[\omega_p(x)t]$ is stationary,[2] that is, the points where one or more derivatives of $[\omega_p(x)t]$ vanish.

Under the assumption that the point $x = x_0$ is such a stationary point, $\omega_p(x)$ may be expanded about this point as follows:

$$\omega_p(x) \approx \omega_p(x_0) + \frac{1}{(n+1)!} \omega_p^{n+1}(x_0)(x-x_0)^{n+1}. \tag{3}$$

In Eq. 3 the first n derivatives of ω_p are assumed to vanish at $x = x_0$. The superscript (n+1) on ω_p in (3) signifies the $(n+1)^{th}$ derivative of $\omega_p(x)$. Using (2) and (3), we find as $t \to \infty$

$$V(t) \approx \frac{-2e\delta n_0(x_0) \, \Gamma\left(\frac{1}{n+1}\right)}{(n+1) \, \epsilon_0 \left[\frac{1}{(n+1)!} \left| \omega_p^{n+1}(x_0) \right| t \right]^{\frac{1}{n+1}}} \cos \left[\omega_p(x_0)t \pm \frac{\pi}{2(n+1)} \right] \qquad \text{n odd} \tag{4}$$

$$V(t) \approx \frac{-2e\delta n_0(x_0) \, \Gamma\left(\frac{1}{n+1}\right)}{(n+1) \, \epsilon_0 \left[\frac{1}{(n+1)!} \left| \omega_p^{n+1}(x_0) \right| t \right]^{\frac{1}{n+1}}} \cos \frac{\pi}{2(n+1)} \cos [\omega_p(x_0)t] \qquad \text{n even} \tag{5}$$

In Eq. 4, the plus sign is used if $\omega_p^{n+1}(x_o) > 0$, and the minus sign if $\omega_p^{n+1}(x_o) < 0$. A general result that can be seen from (4) and (5) is that the voltage decays as $(1/t)^{\frac{1}{n+1}}$, where n is the number of derivatives of $\omega_p(x)$ that vanish at the stationary point $x = x_o$.

To check these general results, consider the density $n_o(x) = \dfrac{n_c}{1+x^2}$. For this distribution, $\omega_p(x)$ has one stationary point at $x = 0$. Only the first derivative vanishes, so $n = 1$. Also, we find that $\omega_p''(0) = -\omega_{pc}$. Using Eq. 4, and the fact that $\Gamma(1/2) = \sqrt{\pi}$, the asymptotic voltage is

$$V(t) \approx -\frac{e\delta n_c}{\epsilon_o} \sqrt{\frac{2\pi}{\omega_{pc}t}} \cos\left[\omega_{pc}t - \frac{\pi}{4}\right],\tag{6}$$

which agrees with Eq. 19 of our previous report,[1] where the asymptotic form of the voltage had been obtained from the explicit solution for $V(t)$.

Finally, we can use (4) to obtain the asymptotic response for the class of distributions

$$n_o(x) = \frac{n_c}{1+x^{2k}}, \qquad k = 1, 2, \ldots,$$

which was also discussed in our previous report.[1] For arbitrary k, it can be shown that $(2k-1)$ derivatives of $\omega_p(x)$ vanish at $x = 0$, and that the first nonvanishing derivative is negative. Hence, Eq. 4 gives for the voltage as $t \to \infty$

$$V(t) \sim \frac{1}{t^{1/2k}} \cos\left[\omega_{pc}t - \frac{\pi}{4k}\right].\tag{7}$$

Overtaking Times for a Special Class of Densities

We have shown previously[3] that in an inhomogeneous plasma where the plasma frequency is $\omega_p(x)$, an overtaking will occur after an initial displacement perturbation in a time that is

$$t_o \approx \frac{1}{\delta\omega_p'}\tag{1}$$

at a point in the plasma defined by

$$\omega_p''(x) = 0.\tag{2}$$

In Eqs. 1 and 2, the primes indicate derivatives with respect to x, and δ is the displacement amplitude.

For the density distributions

$$n_o(x) = \frac{n_c}{1+x^{2k}} \qquad k = 1, 2, \ldots \tag{3}$$

the overtaking occurs at a point given by

$$x_o = \pm \left(\frac{2k-1}{k+1}\right)^{1/2k}, \tag{4}$$

and the time of overtaking is

$$\omega_{pc}t_o = \frac{1}{6}\frac{1}{k}\left(\frac{2k-1}{k+1}\right)^{\frac{1}{2k}-1}\left(\frac{3k}{k+1}\right)^{3/2}. \tag{5}$$

We note that as $k \to \infty$, the density given by (3) approaches that of a uniform plasma, with density n_c distributed between $x = -1$ and $x = +1$. In this limit the plasma has sharp boundaries and (4) predicts that the overtaking occurs at these boundaries $(x_o = \pm 1)$. Equation 5 predicts that the time of overtaking approaches zero in the limit $(k \to \infty)$ of a sharply bounded plasma.

H. M. Schneider, A. Bers

References

1. A. Bers and H. M. Schneider, Quarterly Progress Report No. 89, Research Laboratory of Electronics, M.I.T., April 15, 1968, pp. 123-126.

2. A. Erdelyi, Asymptotic Expansions (Dover Publications, Inc., New York, 1956), p. 52.

3. H. M. Schneider and A. Bers, "Nonlaminar Effects in Plasma Slab Oscillations," Symposium on Computer Simulation of Plasma and Many-Body Problems, Williamsburg, Virginia, April 1967.

5. STABILITY OF ELECTRON BEAMS WITH VELOCITY SHEAR

In high-perveance electron beams, the axial velocity of the electrons generally varies with radius, because of the substantial space-charge potential depression. Many years ago, it was speculated that this multistream configuration might result in growing waves by a two-stream mechanism,[1] but later analyses of infinite beams with spatially independent velocity distributions $f_0(v)$ were invoked as proof of stability in all cases for which $f_0(v)$ is single-peaked.[2] In all available treatments of the actual sheared flow very special velocity profiles have been assumed.[3,4]

In this report, we shall derive two necessary conditions for instability for electron beams focused by infinite magnetic fields. Our approach parallels the general methods used in the stability analysis of parallel flows of inviscid fluids,[5] and indeed it was primarily the analogy with sheared hydrodynamic flows that stimulated our re-evaluation of the electron beam stability.

We consider a slab beam, infinite in the x and z directions, in which the electrons move only in the z direction with a velocity $v_{0z}(y)$. We assume a dependence of $\exp[j(\omega t - kz)]$, where k is real, and, for unstable modes, $\omega \triangleq \omega_r + j\omega_i$ with $\omega_i < 0$. The differential equation for the small-signal potential, ϕ, is

$$\frac{\partial^2 \phi}{\partial y^2} - k^2 \left[1 - \frac{\omega_p^2(y)}{[\omega - k v_{0z}(y)]^2} \right] \phi = 0, \tag{1}$$

where $\omega_p(y)$ is the usual plasma frequency, $\dfrac{\eta \rho_0(y)}{\epsilon_0}$. Using Eq. 1 without making any assumptions about $v_{0z}(y)$ or $\omega_p(y)$, we can derive two necessary conditions for instability ($\omega_i < 0$).

THEOREM 1. A necessary condition for instability is

$$(v_{0z})_{min} < \frac{\omega_r}{k} < (v_{0z})_{max}. \tag{2}$$

Proof: Multiply Eq. 1 by ϕ^* and integrate over all y from $-\infty$ to $+\infty$. Assume $\phi = 0$ at $\pm\infty$. Then

$$\int_{-\infty}^{\infty} \left| \frac{\partial \phi}{\partial y} \right|^2 dy + k^2 \int_{-\infty}^{\infty} |\phi|^2 dy = k^2 \int_{-\infty}^{+\infty} \frac{\omega_p^2 |\phi|^2}{[\omega - k v_{0z}(y)]^2} dy. \tag{3}$$

The imaginary part of Eq. 3 yields

$$k^2 \int_{-\infty}^{+\infty} \frac{2 \frac{\omega_i}{k} \left[v_{0z}(y) - \frac{\omega_r}{k} \right] \omega_p^2(y)}{\left| v_{0z}(y) - \frac{\omega}{k} \right|^4} |\phi|^2 dy = 0. \tag{4}$$

For $\omega_i \neq 0$, this can only be true if Eq. 2 is satisfied, where $(v_{0z})_{min}$ and $(v_{0z})_{max}$ are the maximum and minimum velocities of the beam.

THEOREM 2. A necessary condition for instability is that somewhere over the cross section of the electron beam,

$$\omega_p^2(y) < \frac{1}{4}\left(\frac{\partial v_{0z}(y)}{\partial y}\right)^2 .$$ (5)

Proof: In Eq. 1, let $\phi = \sqrt{v_{0z}(y) - u}\, f$, where $u = \frac{\omega}{k}$. This yields

$$\frac{d}{dy}\left[(v_{0z}-u)f'\right] + f\left\{-k^2(v_{0z}-u) + \frac{1}{2}v_{0z}'' + \frac{\omega_p^2 - \frac{1}{4}(v_{0z}')^2}{v_{0z} - u}\right\} = 0.$$ (6)

Multiply by f^* and integrate by parts over the beam (from $y = y_1$ to $y = y_2$). Again we assume that $\phi \rightarrow 0$ as $y \rightarrow \pm\infty$, or that there are conducting walls (at zero potential) at some finite values of y. Then, the imaginary part of the resulting equation (for $\omega_i \neq 0$) yields

$$\int_{y_1}^{y_2} |f|^2 \left(\frac{\omega_p^2 - \frac{1}{4}(v_{0z}')^2}{|v_{0z}-u|^2}\right) dy < 0.$$ (7)

Since all of the remaining terms are positive definite, Eq. 7 is only satisfied if Eq. 5 is true over at least a portion of the beam.

R. J. Briggs, J. A. Rome

References

1. A. V. Haeff, Proc. IRE 37, 4-10 (1949).

2. L. R. Walker, Appl. Phys. 25, 131 (1954).

3. W. R. Beam, "On the Possibility of Amplification in Space-Charge Potential-Depressed Electron Streams," Proc. IRE 43, 454-462 (1955).

4. E. Hochmair and E. Mondre, "Wave Propagation in Electron Beams Produced by Non-equipotential Cathodes," Final Technical Report (European Research Office), Institut für Hochfrequenztechnik der Technischen Hochschule, Wien, January 1967.

5. P. G. Drazin and L. N. Howard, "Hydrodynamic Stability of Parallel Flow of Inviscid Fluid," Advances in Applied Mechanics, Vol. 9, pp. 1-89, 1966.

XIII. PLASMAS AND CONTROLLED NUCLEAR FUSION

C. Active Plasma Effects in Solids*

Academic and Research Staff

Prof. A. Bers
Prof. G. Bekefi

Prof. S. K. Sharma
Dr. W. M. Manheimer

Graduate Students

E. V. George
C. S. Hartmann

D. A. Platts

J. H. Spencer
R. N. Wallace

1. MICROWAVE INSTABILITIES IN n-InSb SUBJECTED TO DC ELECTRIC AND MAGNETIC FIELDS

We are continuing the investigation of the emission of microwave radiation from n-type InSb when a sample is subjected simultaneously to parallel DC electric and magnetic fields. It has been observed[1] that certain thresholds in DC electric and magnetic fields must be exceeded in order to obtain any microwave emission. This emission consists of discrete spikes superposed on a background continuum. This report illustrates the frequency dependence of the threshold curve. Microwave emission occurs upward and to the right of the threshold curve shown in Fig. XIII-23.

The threshold characteristics for the microwave emission have been studied from 30 MHz up to 3 GHz, and are illustrated in Fig. XIII-23. The open circles represent the threshold for the onset of the spiky emission, while the open triangles represent the threshold for the onset of the continuum radiation. We observed that in the low B-field regime the radiation consisted primarily of noise spikes, while in the high B-field regime the radiation consisted of a very few spikes superposed on a strong background continuum. The onset for this continuum radiation was very abrupt, whereas the onset for the discrete noise spikes was very gradual.

In this work threshold was arbitrarily defined as that amount of microwave emission which is just discernible above receiver noise. In the high B-field regime, since the onset for the radiation was very abrupt, any frequency dependence of the receiver noise would not greatly affect the threshold value of electric field. Whereas in the high E-field regime, since the onset for the radiation (noise spikes) was very gradual, any frequency dependence in the receiver noise will markedly affect the threshold value of magnetic field. Since it was not possible to properly match the impedance of the sample to the receiver at 30 MHz the thresholds for both electric and magnetic field were higher, as seen in Fig. XIII-23. To eliminate this
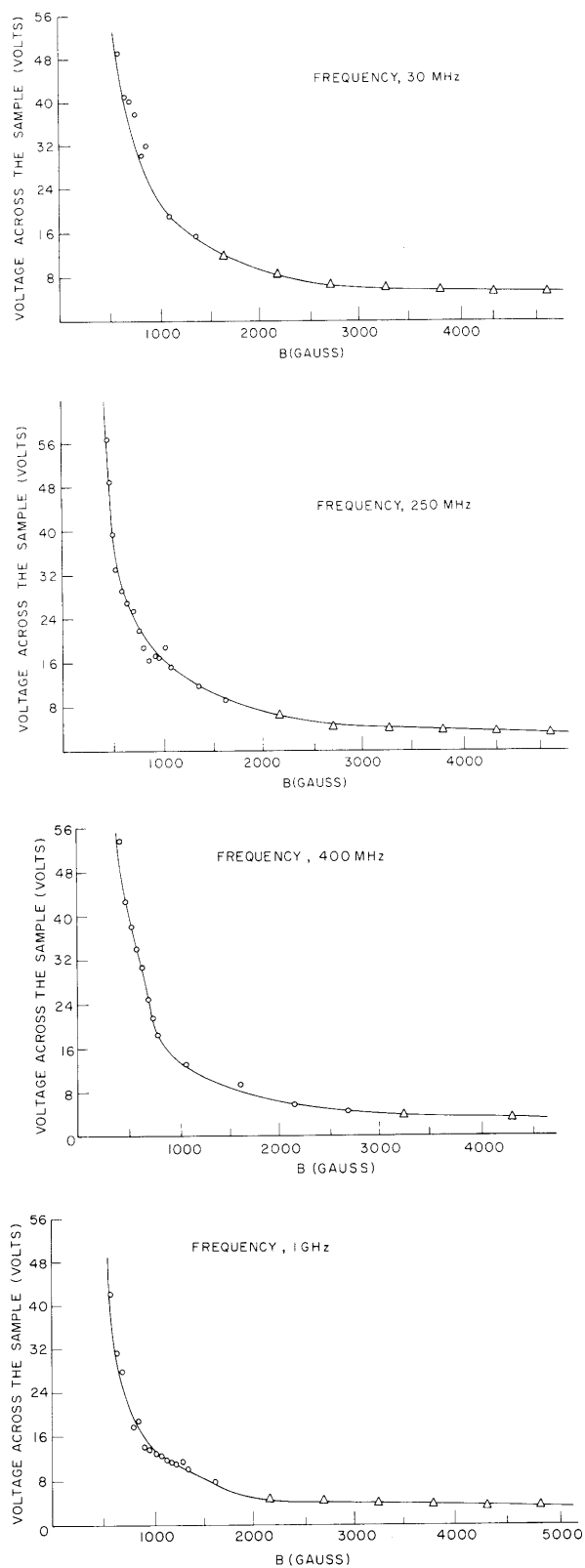
Fig. XIII-23. Threshold electric field vs threshold magnetic field for microwave emission at 77°K for various frequencies of observation. IF bandwidth, 10 MHz.
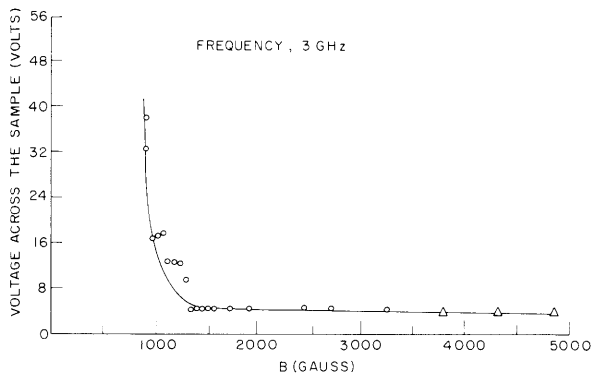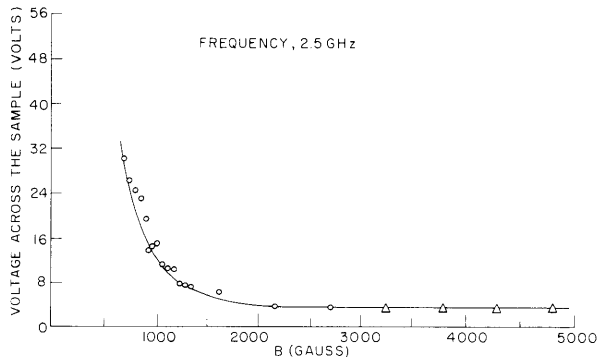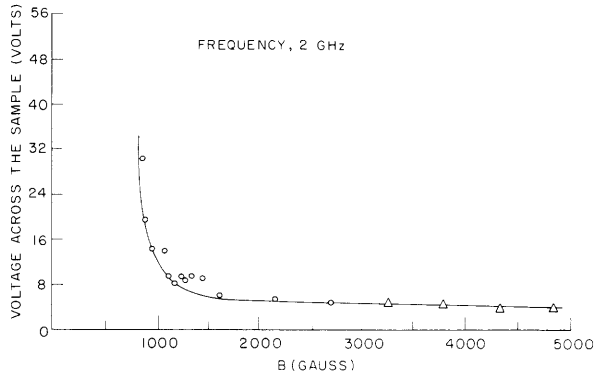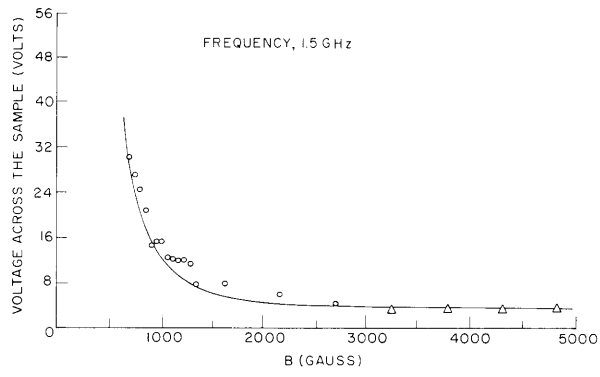
109

Fig. XIII-23.   Concluded.

problem, we are repeating these threshold measurements, using a calibrated noise standard and defining threshold at some equivalent noise temperature T_o.

These measurements were made on a sample (S1-141), 1 mm × 1 mm × 11.2 mm, which had a mobility $\mu = 5.9 \times 10^5$ cm^2 V^{-1} sec^{-1}, and a density n = 2.6 × 10^{14} cm^{-3}. The contacts were made by first electroplating In to the crystal ends and then soldering Au wire with In solder to the plated surfaces. Using this technique for attaching the contacts to our crystals, we found, contrary to the results of our previous work, that the measured conductivity of the crystal agreed, within experimental error, with the manufacturer's published value.

E. V. George

References

1. E. V. George, Quarterly Progress Report No. 88, Research Laboratory of Electronics, M. I. T., January 15, 1968, pp. 202-204.

2. COLLISION-INDUCED INSTABILITY FOR HELICON WAVES

It is well known[1-3] that collisions between the free particles of a gaseous plasma can induce instabilities (i. e., growth) in certain types of transverse electromagnetic and longitudinal plasma waves. In maser language, the conditions for growth[2] are (a) that the population of particle energies be inverted, and (b) that the "weighted" lifetime of the upper state exceed that of the lower state. Requirement (a) is synonymous with the statement that in some range of free-particle energies,

$$\frac{\partial f(v)}{\partial v} > 0, \tag{1}$$

where f(v) is the distribution function for particle speeds. Condition (b) imposes certain properties on the energy dependence of the collision frequency for momentum transfer, $\nu(v)$. In essence it asks that in the regime of particle speeds where Eq. 1 is satisfied, $\nu(v)$ vary with v at a rate that is faster than that prescribed by a certain minimum rate. Whether this variation of $\nu(v)$ with v should be a decreasing or increasing function of v ($\partial \nu / \partial v \gtrless 0$) to obtain an instability, depends on the type of wave and frequency being considered.

In this report we examine the characteristics of the aforementioned instability for the special case of helicon (whistler) wave propagation in a solid. We assume a harmonic wave of the form $\exp(j\omega t - j\vec{k} \cdot \vec{r})$, where ω is the frequency, and $\vec{k}$ the propagation vector. We then solve the appropriate dispersion relation for real k and complex ω ($\omega = \omega_r + j\omega_i$) and examine the unstable regime $\omega_i \leq 0$. We are particularly interested in the properties of the wave at the stability boundary ($\omega_i = 0$) that separates the region

of growing waves from the region of damped waves. We shall find that this stability boundary exhibits (fortuitously or otherwise) several of the properties observed experimentally,[4,5] when a sample of Indium Antimonide is subjected simultaneously to parallel DC electric and magnetic fields.

Wave Propagation Along the Magnetic Field

The dispersion relation has the form

$$k^2 c^2 = \omega^2 K. \tag{2}$$

Here, $K(\omega, \omega_p, \omega_c, f)$ is the dielectric coefficient with $\omega_p^2 = Ne^2/m^* \epsilon_o$ as the plasma frequency, $\omega_c = eB/m^*$ is the electron cyclotron frequency, and m^* is the effective mass of the charged particles (taken to be isotropic). We assume throughout that there is only one mobile species, the electrons. Solving the linearized Boltzmann equation for waves propagating along the magnetic field direction, one then finds[6]

$$K = K_{lattice} + \frac{\omega_p^2}{\omega} \int_0^\infty \frac{1}{(\omega \pm \omega_c) - j\nu(v)} \frac{\partial f}{\partial v} \frac{4\pi}{3} v^3 \, dv, \tag{3}$$

where, for simplicity, we have assumed that the electron velocity distribution function is isotropic (only a function of speed v). The plus and minus signs in Eq. 3 refer to the left- and right-hand circularly polarized waves, respectively. The low-frequency and high-density limits,

$$\omega \ll \omega_c, \qquad \frac{\omega_p^2}{\omega \omega_c} \gg K_{lattice}, \tag{4}$$

characterize helicon wave propagation. It so turns out that both the left- and right-hand polarized waves can propagate in the presence of velocity-dependent collisions and that both waves can exhibit a collision-induced instability. For the purpose of this report, however, we shall consider the right-hand polarized wave only. Thus

$$K \approx -\frac{\omega_p^2}{\omega} \int_0^\infty \frac{1}{\omega_c + j\nu(v)} \frac{\partial f}{\partial v} \cdot \frac{4\pi}{3} v^3 \, dv. \tag{5}$$

To solve Eq. 5 we must choose a specific form for the distribution function. To keep the solution tractable we assume a delta function of the form,

$$f = \frac{1}{4\pi v_o^2} \delta(v - v_o); \qquad \int f d^3v = 1, \tag{6}$$

where, for the lack of a better name, we shall call v_o the electron "drift" velocity. We now substitute Eq. 6 in Eq. 5 and solve the resulting dispersion relation (2) for real k and complex $\omega = \omega_r + j\omega_i$. Assuming that $\left|\omega_i\right| \ll \omega_r$, a condition that is certainly well satisfied at and near the instability boundary $\omega_i = 0$, we obtain for the real and imaginary parts of ω,

$$\frac{k^2 c^2}{\omega_r} = \frac{\omega_c \omega_p^2}{\omega_c^2 + \nu^2(v_o)} \left\{ 1 - 2\left[\frac{v_o}{3} \frac{\nu'}{\nu(v_o)}\right] \frac{\nu^2(v_o)}{\omega_c^2 + \nu^2(v_o)} \right\}$$

(7)

$$\left(\frac{k^2 c^2}{\omega_r}\right)\left(\frac{\omega_i}{\omega_r}\right) = \frac{\omega_p^2\, \nu(v_o)}{\omega_c^2 + \nu^2(v_o)} \left\{ 1 + \left[\frac{v_o}{3} \frac{\nu'}{\nu(v_o)}\right] \frac{\omega_c^2 - \nu^2(v_o)}{\omega_c^2 + \nu^2(v_o)} \right\},$$

(8)

where

$$\nu' \equiv \frac{d\nu(v)}{dv}\bigg|_{v=v_o}.$$

(9)

It follows from Eq. 8 that the instability sets in when

$$\left[-\frac{v_o}{3} \frac{\nu'}{\nu(v_o)}\right] \geqslant \frac{\omega_c^2 + \nu^2(v_o)}{\omega_c^2 - \nu^2(v_o)}.$$

(10)

The equality sign refers to the boundary $\omega_i = 0$ where the system is just marginally stable.
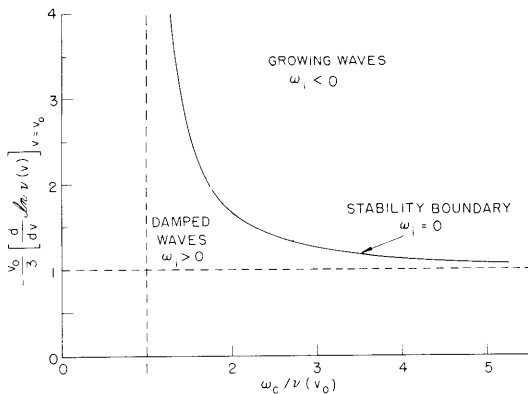

Fig. XIII-24.

Instability characteristics of helicon waves propagating along the direction of the static magnetic field.

Substitution of Eq. 10 (with the equality sign) in Eq. 7 yields the following dispersion relation for waves at the stability boundary:

$$\frac{k^2 c^2}{\omega_r} = \frac{\omega_c \omega_p^2}{\omega_c^2 - \nu^2(v_o)} \qquad (\text{at } \omega_i = 0). \tag{11}$$

The minus sign appearing in this equation is important. We see that as ω_c approaches $\nu(v_o)$ the wavelength tends to zero. We also see that propagating waves can exist only when $\omega_c^2 \geqslant \nu^2(v_o)$. Thus it follows from Eq. 10 that the helicon wave instability requires $\nu' < 0$, namely the collision frequency must decrease with increasing electron speed v_o. Regions of stability and instability are illustrated in Fig. XIII-24. It is noteworthy that the stability boundary is only a function of the strength of the magnetic field and of the collision frequency; it is independent of the frequency of the wave or the plasma density
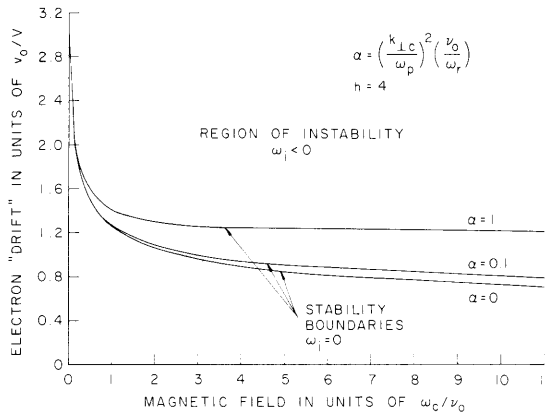

$$\alpha = \left(\frac{k_\perp c}{\omega_p}\right)^2 \left(\frac{\nu_o}{\omega_r}\right)$$

h = 4

REGION OF INSTABILITY
$\omega_i < 0$

$\alpha = 1$

$\alpha = 0.1$

$\alpha = 0$

STABILITY
BOUNDARIES
$\omega_i = 0$

ELECTRON "DRIFT" IN UNITS OF v_o/V

MAGNETIC FIELD IN UNITS OF ω_c/ν_o

Fig. XIII-25.

Stability boundary for helicons propagating along the magnetic field in an unbounded medium ($\alpha = 0$) and for guided helicons ($\alpha \neq 0$) traveling through a sample of effective transverse dimension given by $m\pi/k_\perp$, $m = 1, 2, 3 \ldots$. The exponent h in $\nu \propto v^{-h}$ is set equal to 4.

(provided, of course, that inequalities (4) are obeyed). We shall see that for waves in a plasma of finite dimensions, however, the stability boundary becomes a function of both ω and ω_p.

In order to see the detailed behavior of the stability boundary with varying magnetic field and electron "drift" v_o, we must choose a specific dependence of $\nu(v)$ on v. We assume a power law of the form

$$\nu(v) = \nu_o \left(\frac{V}{v}\right)^h. \tag{12}$$

Here ν_o and V are constants, and h is a positive number that must be greater than 3 for instability, as is readily seen by substituting Eq. 12 in Eq. 10. A plot of the electron "drift" as a function of magnetic field, showing the demarcation between stability and instability, is given in Fig. XIII-25 (by the curve marked $\alpha \equiv (k_\perp c/\omega_p)^2 (\nu_o/\omega_r) = 0$.

Wave Propagation at an Angle to the Magnetic Field (Guided Waves)

The dispersion relation for helicons propagating at an angle to the magnetic field

is complicated, particularly when the solution must be obtained from the Boltzmann equation, as is the case when ν is a function of particle speed. When ν is a constant (and nonlocal effects are neglected) an approximate solution[7] based on the MHD transport equations shows that wherever ω_c appears in the dispersion equation it should be replaced by $\omega_c \cos \theta$, where θ is the angle between the propagation constant $\vec{k}$ and the direction of the magnetic field $\vec{B}$. Such a replacement is valid as long as $\omega \ll \omega_c \cos \theta$.

We assume (with little justification) that what has been shown to be valid in the MHD calculations is likewise valid in the kinetic approach. This has the merit of simplicity, and when ν is a constant, we recover the customarily used dispersion relation for helicons. Thus in Eqs. 4, 5, 7, 8, 10, and 11 we make the replacement

$$\left.\begin{array}{l} \omega_c \rightarrow \omega_c \cos \theta \\[2mm] = \omega_c \dfrac{k_{\parallel}}{k} \\[4mm] = \omega_c \left(1 - \dfrac{k_{\perp}^2}{k^2}\right)^{1/2} \end{array}\right\} \qquad (13)$$

where $k_{\parallel}$ and $k_{\perp}$ are the components of $\vec{k}$ resolved along and perpendicular to the magnetic field, respectively. In Fig. XIII-25 we show a plot of the stability boundary $\omega_i = 0$ for three values of $k_{\perp}$ (the case $k_{\perp} = 0$, $\alpha = 0$ has been discussed already). By holding $k_{\perp}$ constant and allowing $k_{\parallel}$ to take on any value consistent with Eqs. 10, 11, and 13, we are in fact considering the model of a guided helicon wave traveling in a sample of finite transverse dimensions W such that $k_{\perp} W \approx m\pi$ $(m = 1, 2, \ldots)$. Observe that when $k_{\perp} \neq 0$ the stability boundary does depend (albeit not very strongly) on the particular choice of ω and ω_p.

Standing Waves (Cavity Modes)

In an infinite unbounded medium, the collision-induced instability discussed above is convective[8] which corresponds to spatial amplification over a range of real frequencies. This is the situation discussed above. Suppose, however, that we have a sample of material of finite length L (as well as width W as previously described), and that the growing waves are reflected at the ends. If the reflection coefficient at the boundary is large enough, the reflected wave provides an internal feedback and the system can behave as an oscillator; this, in effect, is like an absolute instability, and corresponds to growth in time at every point in space. Thus very large amplitude signals could build up from noise at certain discrete frequencies at which standing waves are set up. We consider this situation below.

Let L be the length of the sample in the direction of the DC magnetic field
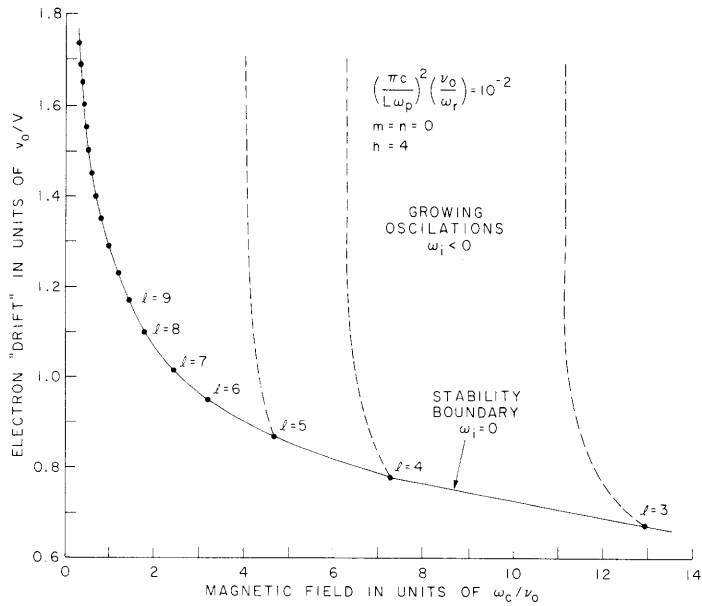
Fig. XIII-26. Stability boundary for standing oscillations (cavity modes) in a sample whose transverse dimensions are large compared with its length L measured along the magnetic field. The exponent h in $\nu \propto v^{-h}$ is set equal to 4. Dashed lines show the path taken by the modes as one proceeds from the stability boundary into the unstable regime.
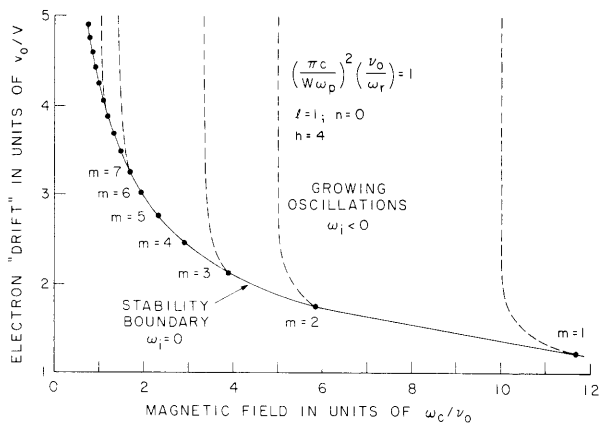

Fig. XIII-27. Stability boundary for standing oscillations (cavity modes) in a sample whose length L is large compared with its width W measured transversely to the magnetic field (the width W in this figure is 1/10 the length L of Fig. XIII-26, with all other parameters held the same). Dashed lines: same as in Fig. XIII-26.

(and $k_\parallel$), and let W and T be its width and thickness perpendicular to the magnetic field, respectively. Then for cavity resonances to occur, we have

$$k_\parallel = \frac{\pi \ell}{L}; \qquad k_x = \frac{\pi m}{W}; \qquad k_y = \frac{\pi n}{T}$$

and

$$\cos \theta = \frac{\dfrac{\ell}{L}}{\left[\dfrac{\ell^2}{L^2} + \dfrac{m^2}{W^2} + \dfrac{n^2}{T^2} \right]^{1/2}}$$

(14)

where ℓ, m, and n are positive integers. Using Eq. 14 in conjunction with relations (10), (11) and (13), we can compute the mode structure of growing standing oscillations along the stability boundary $\omega_i = 0$. This structure is shown in Figs. XIII-26 and XIII-27 by heavy dots. Figure XIII-26 illustrates the case of very large transverse dimensions $W = T \to \infty$, whereas Fig. XIII-27 shows the situation for a sample whose width W is small compared with its length L (in going from Fig. XIII-26 to Fig. XIII-27 we took $L/W = 10$).

Discussion

The collision-induced instability for helicons described above has a number of characteristics that qualitatively resemble the microwave and radio-frequency emission of noise observed[4,5] when a sample of Indium Antimonide is subjected simultaneously to parallel DC electric (E) and magnetic fields (B). The similarities are the following.

(i) Plots of experimentally derived threshold curves of E against B for onset of noise are similar to our calculated stability boundaries of "drift" velocity v_0 vs B.

(ii) The observed emission[5] comprises discrete narrow-bandwidth spikes and broad-band "continuum" radiation. The observed spikes trace out a threshold curve of E vs B similar to our stability boundary for standing waves (Figs. XIII-26 and XIII-27).

(iii) The measured[5] threshold curves are very insensitive to the frequency of observation of the radiation from 30 MHz to 3000 MHz. The theoretical threshold curves are likewise insensitive.

(iv) Measurements show[5] very few spikes at large magnetic fields and many at low magnetic fields. The distribution of resonances shown in Figs. XIII-26 and XIII-27 are qualitatively similar to those observed.

A detailed comparison between theory and experiment has yet to be made. To make such a comparison meaningful, several improvements in the theory are necessary. The functions f(v) and $v(v)$ given by Eqs. 6 and 12 will have to be replaced by quantities that are more closely related to the physical conditions of the experiment. Furthermore, since it appears that helicons propagating at a fairly large

angle to the mangetic field play an important role, the approximations $\omega_c \to \omega_c \cos \theta$ and $\omega \ll \omega_c \cos \theta$ will have to be replaced by a more exact solution of the dispersion relation.

G. Bekefi

Footnotes and References

1. G. Bekefi, J. L. Hirshfield, and S. C. Brown, Phys. Fluids 4, 173 (1961).
2. G. Bekefi, "Radiation Processes in Plasmas" (John Wiley and Sons, Inc., New York, 1966), pp. 306-310.
3. J. M. Wachtel and J. L. Hirshfield, Phys. Rev. Letters 19, 293 (1967).
4. G. Bekefi, A. Bers, and S. R. J. Brueck, Phys. Rev. Letters 19, 24 (1967); also IEEE Trans., Vol. ED-14, p. 593, 1967.
5. See Sec. XIII-C.1.
6. W. P. Allis, "Motions of Ions and Electrons," Handbuch der Physik, Vol. 21 (Springer-Verlag Berlin, 1956), p. 383.
7. E. Legéndy, Phys. Rev. 135, A1713 (1964).
8. An absolute instability sets in when the following conditions can be satisfied simultaneously: $D(\omega, \vec{k}) = 0$, $\partial D(\omega, \vec{k})/\partial k = 0$, where the first relation represents the dispersion relation for the wave in question. For the helicon instability discussed here these conditions are satisfied only at $\omega = 0$, $k = 0$, with the result that this absolute instability at zero real frequency (ω_r) has also zero growth rate ($\omega_i = 0$). Hence it appears that this singular point in the frequency domain need not concern us further.

3. ACOUSTIC WAVE PROPAGATION AND AMPLIFICATION IN InSb

We are continuing our studies of acoustic wave amplification at microwave frequencies, using high-mobility acoustically active materials in applied electric and magnetic fields. In this report we describe the acoustic wave propagation characteristics in InSb, and its relevant elastic parameters that enter into the gain formulation given previously.[1,2]

The acoustic modes of any elastic solid are solutions of the following equations.[3]

$$\rho \frac{\partial^2 u_i}{\partial t^2} = \frac{\partial T_{ij}}{\partial x_j} \qquad (1)$$

$$T_{ij} = C_{ijk\ell} S_{k\ell} = C_{ijk\ell} \frac{1}{2} \left[\frac{\partial u_k}{\partial x_\ell} + \frac{\partial u_\ell}{\partial x_k} \right], \qquad (2)$$

where ρ is the mass density, u_i is the "i"th component of acoustic material displacement, T_{ij} is the stress, $S_{k\ell}$ is the strain, $C_{ijk\ell}$ is the elastic tensor, and x_k is a coordinate direction. In contracted subscript notation,[4] Hooke's law is written

$$T_i = C_{ij} S_j. \tag{3}$$

In this notation, the elastic tensor for a cubic crystal structure such as InSb is

$$\overline{\overline{C}} = \begin{bmatrix} C_{11} & C_{12} & C_{12} & 0 & 0 & 0 \\ C_{12} & C_{11} & C_{12} & 0 & 0 & 0 \\ C_{12} & C_{12} & C_{11} & 0 & 0 & 0 \\ 0 & 0 & 0 & C_{44} & 0 & 0 \\ 0 & 0 & 0 & 0 & C_{44} & 0 \\ 0 & 0 & 0 & 0 & 0 & C_{44} \end{bmatrix} \tag{4}$$

For InSb the elastic constants that enter into Eq. 4 are[5]

$$C_{11} = 6.66 \times 10^{10} \text{ nt/m}^2$$

$$C_{12} = 3.35 \times 10^{10} \text{ nt/m}^2 \tag{5}$$

$$C_{44} = 3.14 \times 10^{10} \text{ nt/m}^2.$$

If we assume wave solutions of the form $\exp(j\omega t - j\overline{q} \cdot \overline{r})$, we shall find that for any one direction of $\overline{q}$ there will exist 3 orthogonal waves (modes) with 3 corresponding wave velocities that are independent of frequency. In isotropic material one of the modes is always longitudinal, that is, a compression wave with material motion parallel to the direction of propagation (see Fig. XIII-28a). The two remaining modes are shear waves or transverse waves having material motion perpendicular to the direction of propagation (see Fig. XIII-28b).
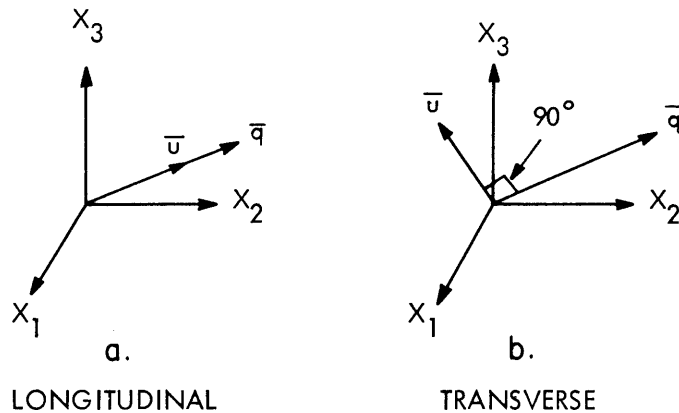

Fig. XIII-28. Longitudinal and transverse waves in isotropic materials.

Since InSb is anisotropic, pure transverse and pure longitudinal waves exist only if the direction of propagation is along one of the high symmetry axes. For an arbitrary direction of propagation, however, there always exists one mode that has its material motion nearly parallel to the direction of propagation and thus is referred to as the longitudinal mode. The two remaining modes are called transverse waves, since their material displacement is nearly perpendicular to the direction of propagation. These two modes are distinguished by their velocities and are referred to as fast or slow transverse waves.
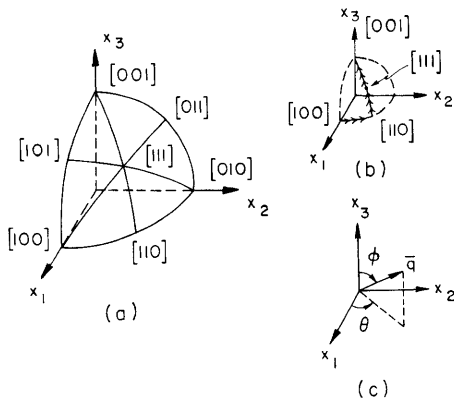

Fig. XIII-29. Directions of wave propagation considered here.

Because of the symmetry of InSb, we need only consider 1/48 of all the possible directions of wave propagation. Figure XIII-29a shows one octant of space divided into 6 equivalent regions. In this figure, spatial directions are indicated by points on the surface of a sphere. The direction is given by the radius vector to that point. The two arcs shown in Fig. XIII-29b indicate the directions for which the equations were solved. Note that the arc from [111] to [001] is equivalent to the arc from [111] to [100]. This choice of directions gives the solution for the entire boundary of one of the symmetrical regions. Figure XIII-30 shows the propagation velocities for all three modes for these directions of propagation. The abscissa of Fig. XIII-30 is labeled in terms of the angles θ and ϕ as defined in Fig. XIII-29c.

Since the crystal structure of InSb lacks a center of symmetry, it exhibits piezo-electricity. The piezoelectric polarization[4] caused by a strain S_j is given by

$$P_i = e_{ij} S_j. \tag{6}$$

The piezoelectric tensor for InSb is

$$\overline{\overline{e}} = \begin{bmatrix} 0 & 0 & 0 & e_{14} & 0 & 0 \\ 0 & 0 & 0 & 0 & e_{14} & 0 \\ 0 & 0 & 0 & 0 & 0 & e_{14} \end{bmatrix}. \tag{7}$$
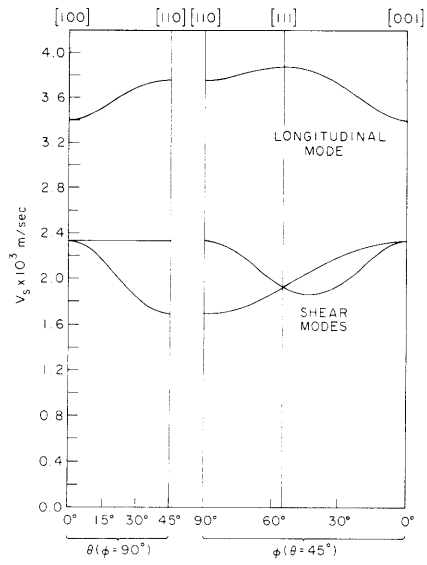
Fig. XIII-30.

Propagation velocities for all three modes in InSb as a function of the direction of $\bar{q}$.
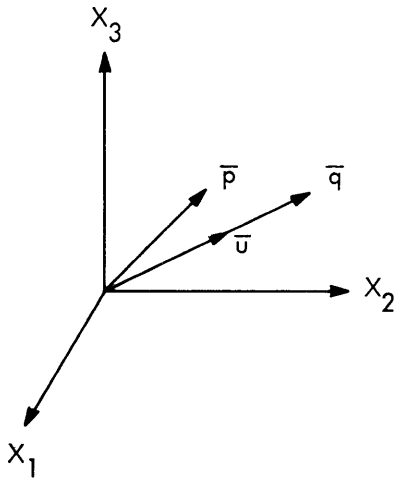
Fig. XIII-31.

Piezoelectric polarization accompanying a longitudinal wave.
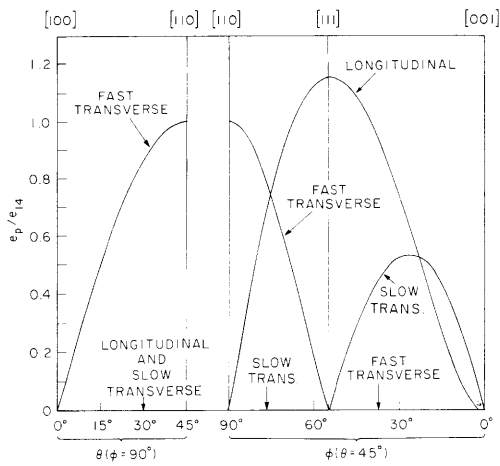
Fig. XIII-32.

Longitudinal effective piezoelectric constant as a function of the direction of $\bar{q}$.

121
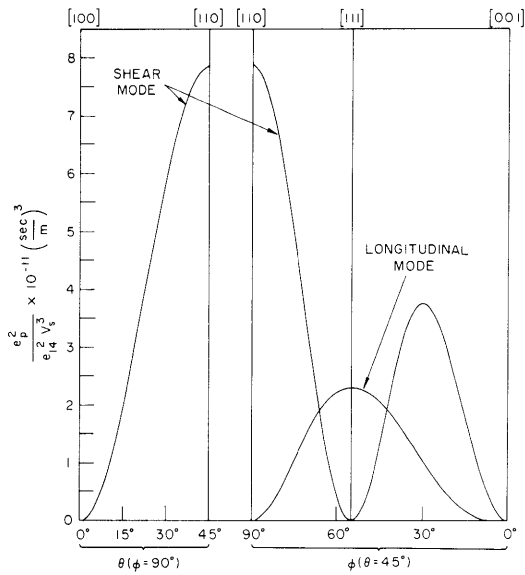
Fig. XIII-33.

Gain in relative units as a function of
the direction of $\overline{q}$ for $\omega < \omega_{max}$.

Fig. XIII-34.

Gain in relative units as a function of the
direction of $\overline{q}$ for $\omega = \omega_{max}$.

Fig. XIII-35.

Gain in relative units as a function of the direction
of $\overline{q}$ for $\omega > \omega_{max}$.

The measured value of $e_{14} = 0.06$ coul./m^2.[6]

An acoustic wave has a strain associated with it whose magnitude is given by the product of $|\bar{\mu}|$ and $|\bar{q}|$. The spatial direction of the polarization induced by this strain has no simple relation to the direction of propagation (see Fig. XIII-31). The lo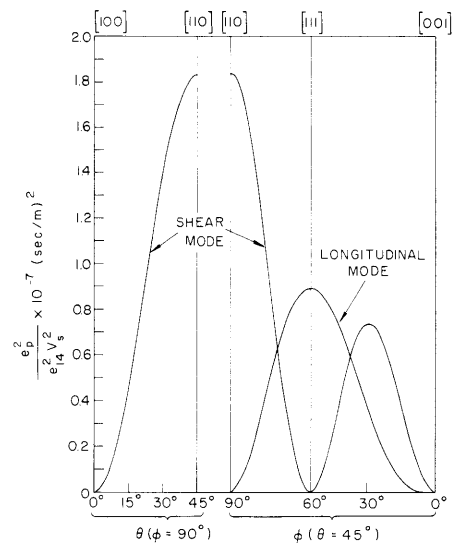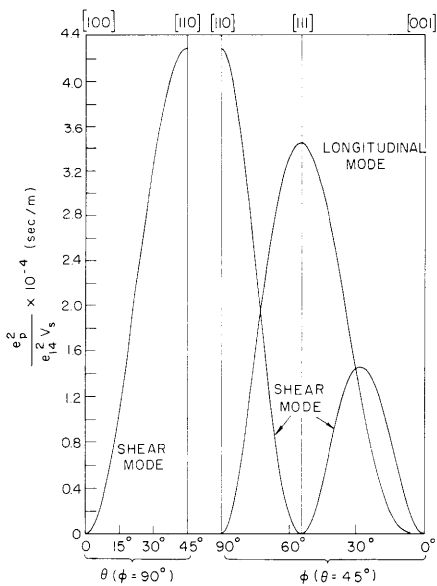ngitudinal component of $\bar{P}$ (the component parallel to $\bar{q}$) is the only part of interest here and thus one defines a longitudinal effective piezoelectric coefficient e_p as follows.

$$\frac{\bar{P} \cdot \bar{q}}{|q|} = e_p |\bar{\mu}| \, |\bar{q}| \tag{8}$$

Figure XIII-32 shows e_p/e_{14} for all three modes for the same directions of propagation used in Fig. XIII-30.

The longitudinal effective piezoelectric constant is of interest because this component couples the acoustic wave to free electrons in a manner that can lead to acoustic amplification if the free electrons have the proper DC drift velocity.[1] Previously, the growth rate has been given[1] as

$$q_i = \frac{1}{2} \cdot \frac{e_p^2 \omega_o}{V_s^3 \rho \epsilon_L} \cdot \frac{b_\ell \delta}{\delta^2 + b_\ell^2 \left(\dfrac{\omega_o}{\omega} + \dfrac{\omega}{\omega_D}\right)^2}, \tag{9}$$

where b_ℓ and δ are factors depending on the direction and magnitude of the applied electric and magnetic fields, V_s is the sound velocity, ϵ_L is the lattice dielectric constant, $\omega_o = \dfrac{\sigma_o}{\epsilon_L}$, σ_o is the DC conductivity, $\omega_D = V_s^2/D$, and D is the diffusion constant. This equation has a maximum with respect to ω and also with respect to b_ℓ and δ.[1,2] Using these results, we find that the elastic properties of the material enter differently into the maximum gain expression for different frequency regimes:

$$q_i \propto \begin{cases} \dfrac{e_p^2}{v_s^3}; & \omega < \omega_{max} \\[3ex] \dfrac{e_p^2}{v_s^2}; & \omega = \omega_{max} \\[3ex] \dfrac{e_p^2}{v_s}; & \omega > \omega_{max} \end{cases} \tag{10}$$

where $\omega_{max} = (\omega_o \omega_D)^{1/2}$. Figures XIII-33, XIII-34, and XIII-35 show the relative gain

parameters of Eq. 10 as a function of the angle of propagation. We note that the gain is largest for the piezoelectrically active shear wave propagating in the [110] direction.

C. S. Hartmann, A. Bers

References

1. A. Bers, Quarterly Progress Report No. 88, Research Laboratory of Electronics, M. I. T. , January 15, 1968, pp. 204-209.

2. D. A. Platts and A. Bers, Quarterly Progress Report No. 89, Research Laboratory of Electronics, M. I. T. , April 15, 1968, pp. 164-167.

3. L. D. Landau and E. M. Lifshitz, Theory of Elasticity (Addison-Wesley Publishing Co. , Inc. , Reading, Mass. , 1959).

4. W. P. Mason, Piezoelectric Crystals and Their Application to Ultrasonics (D. Van Nostrand Co. , Inc. , New York, 1950).

5. R. F. Potter, Phys. Rev. 103, 47 (1956).

6. K. W. Nill, Ph. D. Thesis, Department of Electrical Engineering, M. I. T. , May 1966.

4. SLOW HELICON PROPAGATION IN PERIODIC SEMICONDUCTOR STRUCTURES

Introduction

In its simplest form, the helicon[1] is essentially a circularly polarized TEM wave propagating along a static magnetic field in a semiconductor or metal. The phase velocity of the wave is reduced far below the usual free-space value because the free carriers in the material produce an effective dielectric constant much greater than unity. A helicon may suffer only slight attenuation as it propagates through a material, even when the wave frequency ω is small compared with the collision frequency ν, provided the static magnetic field is sufficiently strong that the cyclotron frequency ω_c of the free carriers satisfies the condition $\frac{\omega_c}{\nu} \gg 1$. The simple helicon may propagate in materials having a single species of free carriers, either electrons or holes, as well as in materials in which both free electrons and holes are present. The circular polarization of the wave is of the same sense as the gyrations of the majority carriers about the static magnetic field.

It is well known[2] that the phase velocity of an electromagnetic wave propagating through a structure that is spatially periodic in the direction of propagation may be much smaller than the phase velocity of a similar wave in an unbounded medium. This concept may be extended to helicon waves propagating through spatially periodic semiconductor structures. The "slow" helicon waves supported by such structures could form the basis for carrier-wave interactions in semiconductors at microwave frequencies.

In principle, carrier drift velocities much smaller than those that are necessary in an unbounded structure could provide useful gain in a periodic structure. It was with these ideas in mind that the analysis described here was undertaken.

Analysis of Helicon Propagation in a Simple Periodic Structure

Figure XIII-36 shows a simple periodic structure in which slow helicon propagation can be analyzed. The structure is composed of semiconductor slabs in which a single free-carrier species, nominally taken to be electrons, is present. Slabs having free-carrier concentration n_1 and thickness aL alternate with slabs of concentration n_2 and thickness $(1-a)L$, where $0 < a < 1$, to give a spatial period of length L. Free carriers in the slabs may be undrifted, or a z-directed electric field may be applied to give them a finite drift velocity. A static magnetic field is applied in the z direction, perpendicular to the interfaces between the slabs. The structure is assumed to be unbounded in the x and y directions.

As the first step in the analysis of the structure, propagation of helicon waves in an unbounded spatially uniform n-type semiconductor will be considered. The resulting "infinite medium" solutions are then combined with appropriate boundary conditions to yield solutions in the periodic structure. Maxwell's equations, together with a simple transport model for the electrons, form the basis for the linearized solution.[3]
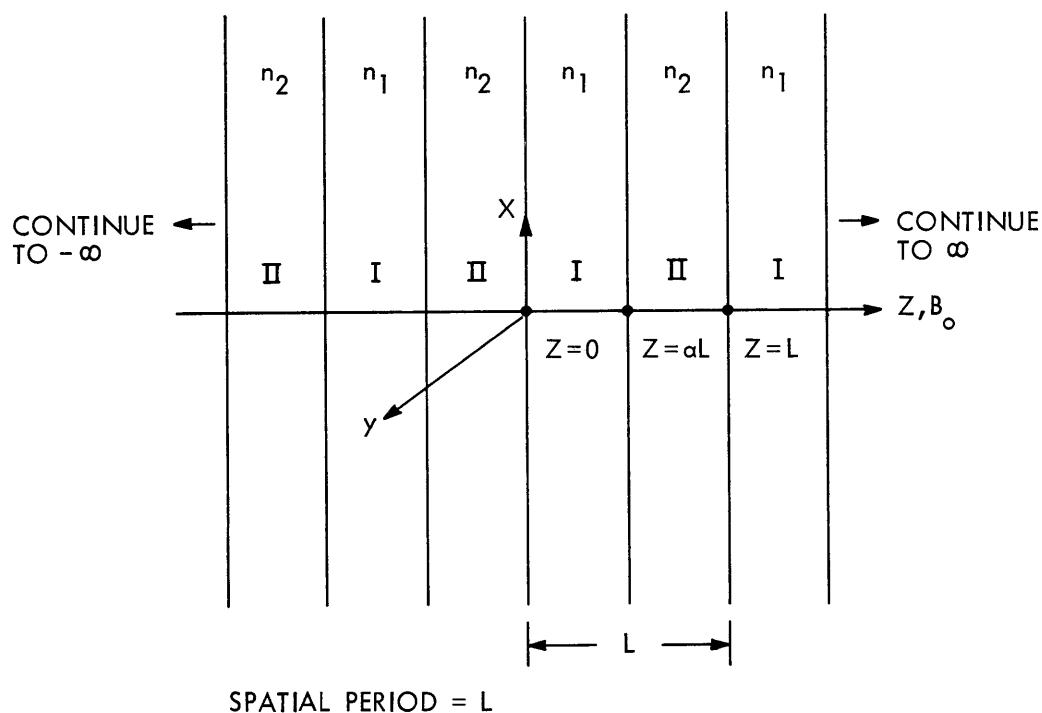

SPATIAL PERIOD = L

Fig. XIII-36. Semiconductor structure supporting slow helicon waves.

Assuming nondrifting electrons, one can write

$$\nabla \times \overline{E}_1 = -\mu_o \frac{\partial \overline{H}_1}{\partial t} \tag{1}$$

$$\nabla \times \overline{H}_1 = \epsilon_L \frac{\partial \overline{E}_1}{\partial t} + \overline{J}_1 \tag{2}$$

$$\frac{\partial \overline{v}_1}{\partial t} = \frac{e}{m^*} \left[\overline{E}_1 + \overline{v}_1 \times \overline{B}_o \right] - \nu \overline{v}_1 \tag{3}$$

$$\overline{J}_1 = n_o e \overline{v}_1. \tag{4}$$

In these equations, the subscript o denotes a steady-state or DC parameter, while the subscript 1 denotes a small-signal variable. The parameters used in these equations are identified below.

$\overline{E}_1$ first-order electric field

$\overline{H}_1$ first-order magnetic field

$\overline{J}_1$ first-order current density

μ_o permeability of free space

ϵ_L lattice permittivity (assumed isotropic)

$\overline{v}_1$ first-order electron velocity

e electron charge

m^* effective electron mass (assumed isotropic)

ν phenomenological collision frequency

n_o density of conduction electrons

$\overline{B}_o$ static magnetic field.

One then assumes wave solutions in which all first-order quantities vary as $\exp[j(\omega t - \overline{q} \cdot \overline{r})]$. After the wave vector $\overline{q}$ is taken along the z-axis, and the solution is specialized to the case of a right-circularly polarized TEM wave ($E_{1y} = -j E_{1x}$, $\overline{q} \cdot \overline{E}_1 = \overline{q} \cdot \overline{H}_1 = 0$), Eqs. 1-4 yield the dispersion relation:

$$q^2 = \frac{\omega^2}{c^2} \left[1 + \frac{\omega_p^2}{j\omega\{(j\omega+\nu)-j\omega_c\}} \right], \tag{5}$$

where $c = \dfrac{1}{\sqrt{\mu_o \epsilon_L}}$ is the phase velocity of light through the lattice, $\omega_p^2 = n_o e^2 / m^* \epsilon_L$

is the square of the electron plasma frequency, and $\omega_c = -eB_o/m^*$ is the electron-cyclotron frequency.

In treating helicons it is usual to make the additional assumptions $\dfrac{\omega_c}{\nu} \gg 1$, $\dfrac{\omega_c}{\omega} \gg 1$

and $\dfrac{\omega_p^2}{\omega \omega_c} \gg 1$. Equation 5 may then be written in the approximate form

$$q^2 = \frac{\omega^2}{c^2} \left(\frac{\omega_p^2}{\omega \omega_c} \right) \left(1 - j \frac{\nu}{\omega_c} \right). \tag{6}$$

For simplicity in the analysis that follows, losses will be neglected so that one may write

$$q^2 = \frac{\omega^2}{c^2} \left(\frac{\omega_p^2}{\omega \omega_c} \right). \tag{7}$$

Note that diffusion effects have been neglected throughout the analysis. This is justified for the particular case treated here because there is no fluctuation in electron density associated with the propagation of the helicon wave.

There are limitations on the transport theory used here beyond the obvious ones imposed by the approximations made to obtain Eq. 7. Effects depending on the detailed nature of the electron velocity distribution are ignored. In particular, Landau damping becomes important when $qv_T \sim \nu$, where v_T is the electron thermal velocity. Also, cyclotron damping is expected to be important when $\omega_c - qv_T < \omega < \omega_c + qv_T$. For the purposes of the analysis presented here, the validity of the transport theory is ensured by the conditions $qv_T \ll \nu$ and $\omega < \omega_c - qv_T$.

The field solution in the periodic structure of Fig. XIII-36 can now be considered. By Floquet's theorem,[2] the general form of the solution for a particular field component must be $F(z) \exp[j(\omega t - \beta_o z)]$, where $F(z)$ is a periodic function having the same spatial period as the structure that is being analyzed.

$$F(z) = F(z-nL) \qquad \text{for any integer } n. \tag{8}$$

The function $F(z)$ may be written in a Fourier series of period L,

$$F(z) = \sum_n A_n \exp\left[-j\left(\frac{2n\pi}{L}\right) z \right], \tag{9}$$

so that the solution for one field component, for example E_{1x}, may be written

$$E_{1x} = e^{j(\omega t - \beta_o z)} \sum_n A_n e^{-j\frac{2n\pi}{L}z} = e^{j\omega t} \sum_n A_n e^{-j\beta_n z}, \tag{10}$$

where $\beta_n = \beta_o + \frac{2n\pi}{L}$. The individual terms or "space harmonics" of Eq. 10 represent physically real components of the actual field solution. Clearly, a knowledge of β_o implies a knowledge of the propagation constants of all space harmonics of the periodic structure.

A solution of the form required by Floquet's theorem can be built up from the "infinite medium" helicon solutions appropriate to the two semiconductor media composing the periodic structure. From Eq. 7 there are two permitted plane-wave solutions in each medium. If one requires the tangential electric and magnetic fields to be continuous at the interfaces between media and further imposes the periodicity condition (8), then a determinantal equation in β_o is obtained. The form is

$$\cos(\beta_o L) = \frac{(q_1+q_2)^2 \cos\left[(\alpha q_1 + (1-\alpha)q_2)L\right] - (q_1-q_2)^2 \cos\left[(\alpha q_1 - (1-\alpha)q_2)L\right]}{4q_1 q_2}. \tag{11}$$

Here,

$$q_i = \left(\frac{\omega^2}{c^2} \frac{\omega_p^2}{\omega \omega_c}\right)_i^{1/2}$$

is the propagation constant for helicons in the ith medium. Equation 11 constitutes the dispersion relation from which all of the space harmonics of the periodic structure can be determined.

General Features of Helicon Propagation in the Periodic Structure

Figure XIII-37 shows a normalized plot of the dispersion relation Eq. 11 for the case $\alpha = 0.5$ and $\frac{q_2}{q_1} = \sqrt{\frac{n_2}{n_1}} = 1.7$. (It has been assumed that the only difference between the two media, I and II, in the periodic structure is in their electron concentrations.) The qualitative features of the dispersion relation remain similar for a wide range of the parameters α and q_2/q_1, so this figure serves well as the basis for a general description. The abscissa gives values of $\beta_o L$, representing the wave vector for the system. The ordinate is marked in units of $(q_1 L)^2 = \omega\left(\omega_p^2/c^2\omega_c\right)_1 L^2$, and thus is a frequency scale.

Only real values of β_o are shown in Fig. XIII-37. Gaps in $\beta_o(\omega)$ correspond to stop bands in which β_o, for the lossless model used here, becomes imaginary. Within a stop

band, the structure supports only evanescent waves. Transitions from a stop band to a passband occur when $\cos(\beta_0 L) = \pm 1$. Physically, these transitions correspond to the
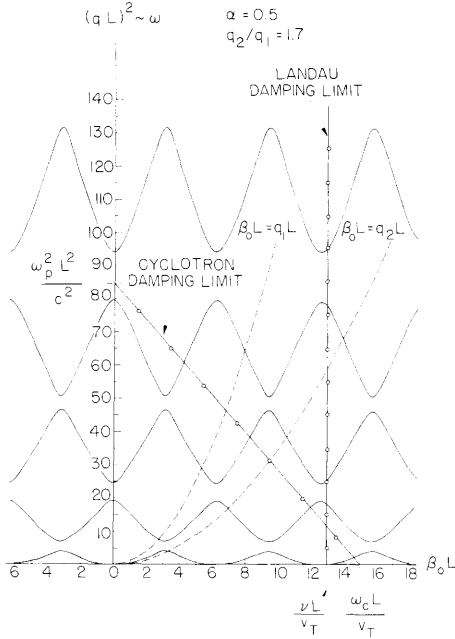

Fig. XIII-37.   Normalized dispersion relation for the periodic structure.

simultaneous establishment of a pole or zero of the wave impedance, E_x/H_y, in the plane $z = aL/2$ and a pole or zero of the wave impedance in the plane $z = (1+a)\frac{L}{2}$. Occasionally, a particular choice of the parameters a and q_2/q_1 leads to a degenerate situation in which two adjacent passbands merge. In general, it is found that the width of the stop bands relative to the passbands increases as the difference in electron density from medium I to medium II increases. This is reasonable, since stronger reflections occur at an interface between markedly different media.

From Fig. XIII-37 it is clear that $\omega(\beta_0)$ is a periodic function of β_0. Both forward $\left(\dfrac{\omega}{\beta_0} > 0,\ \dfrac{\partial\omega}{\partial\beta_0} > 0\right)$ and backward $\left(\dfrac{\omega}{\beta_0} > 0,\ \dfrac{\partial\omega}{\partial\beta_0} < 0\right)$ waves occur in the system, because of the continuous periodic variation of $\omega(\beta_0)$. Also, if one notes that ω cancels out of the factors $(q_1+q_2)^2/4q_1q_2$ and $(q_1-q_2)^2/4q_1q_2$ in Eq. 11, it is apparent that $\beta_0(\omega)$ is a periodic function $\sqrt{\omega}$ whenever $\dfrac{aq_1 + (1-a)q_2}{aq_1 - (1-a)q_2}$ is a rational number.

It is interesting to compare the propagation constants of the helicon waves in media I and II with β_0 as given by the dispersion relation (11). The "infinite medium" solutions are indicated by dashed lines in Fig. XIII-37. One finds empirically for $-\dfrac{\pi}{L} < \beta_0 < \dfrac{\pi}{L}$ that β_0 in the first passband lies close to a weighted average of q_1 and q_2. The approximate relation

$$\beta_0 \approx \alpha q_1 + (1-\alpha)q_2 \tag{12}$$

holds reasonably well. Similarly, this approximate relation gives values close to β_0 in the second passband for $-\frac{2\pi}{L} < \beta_0 < -\frac{\pi}{L}$ and $\frac{\pi}{L} < \beta_0 < \frac{2\pi}{L}$, and values close to β_0 in the third passband for $-\frac{3\pi}{L} < \beta_0 < -\frac{2\pi}{L}$ and $\frac{2\pi}{L} < \beta_0 < \frac{3\pi}{L}$. The intersections of the approximation for β_0 with the lines $\beta_0 L = \pi,\ 2\pi,\ 3\pi \ldots$ give reasonably good values for the locations of the stop-band centers. The approximation becomes progressively worse as α and q_2/q_1 deviate from the values 0.5 and 1.0, respectively. The form of the weighted average suggests that each wave vector q_i contributes to β_0 in proportion to that fraction of the spatial period over which it is effective. An inspection of Eq. 11 shows, in fact, that Eq. 12 becomes exact as $q_1 \to q_2$. The relation

$$\beta_0 \approx \sqrt{\alpha q_1^2 + (1-\alpha)q_2^2} \ ,$$

suggested by an expansion of Eq. 11 for small arguments of the cosine terms, is much less useful than Eq. 12, since it is valid only over a restricted region near the origin.

The limits imposed on the solution by Landau and cyclotron damping are also indicated in Fig. XIII-37. Solutions for ω and β_0 positive are correctly given by the transport theory, as long as they lie well within the boundaries shown. It is also true, of course, that the solution fails unless the predicted wavelengths are long compared with the lattice constant of the semiconductor crystal used. This proves to be a less important restriction in practice than those imposed by Landau and cyclotron damping.

Specialization of Results to the Case of n-InSb at 77°K

Previous work[4] suggests that helicon propagation through the periodic structure of Fig. XIII-36 will be stable in the presence of carrier drift, provided a single free-carrier species is present. A detailed investigation of the structure with drifting carriers should be made to settle this question. It seems quite possible, however, that the slow helicon waves supported by a periodic semiconductor structure may interact with an adjacent drift current to produce useful gain. To get some idea of the actual parameters involved in this interaction, values representing n-InSb at 77°K will be used.

Figure XIII-38 shows a prototype system in which an interaction with slow helicon waves might be achieved. Microwave coupling circuits, not specified in detail, serve to transfer electromagnetic waves to and from the periodic structure where the helicons propagate. A separate semiconductor slab in which electrons drift under the influence of a DC electric field is placed beside the periodic structure. From simple mode-coupling ideas one might expect that space-charge waves on the drifting electron stream would interact with the fringing fields from the slow helicon waves. With sufficiently strong coupling and low system losses, growth of the helicon waves could occur. The
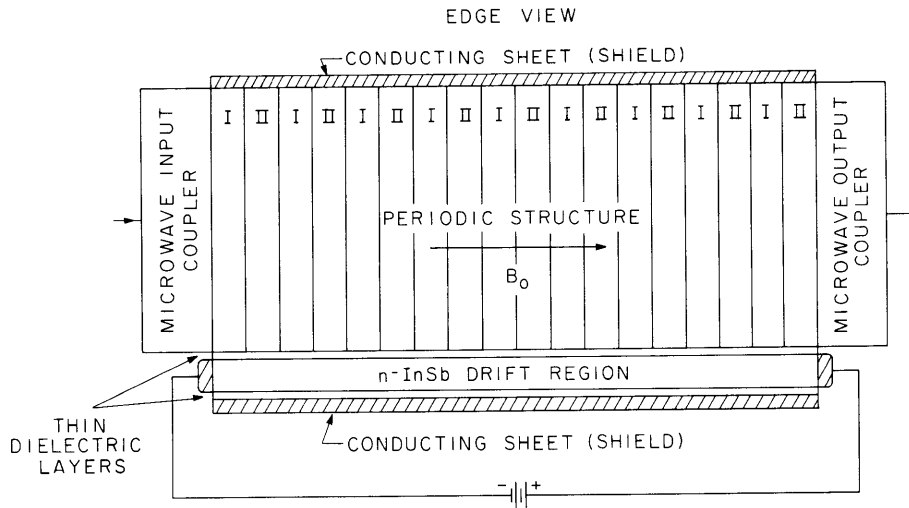
EDGE VIEW

Fig. XIII-38. Prototype structure for obtaining interactions with slow helicon waves.

drift energy of the electron stream would provide the energy necessary to increase the helicon wave amplitude.

A number of comments concerning this interaction should be made. First, the periodic structure must contain a large number of spatial periods, perhaps more than 10 or 20, if its propagation characteristics are to be similar to those found for the infinitely long structure of Fig. XIII-36. Second, previous experience with helicon propagation[5,6] indicates that the phase velocity along the magnetic field is increased as the transverse dimensions of the structure are reduced. The width of the periodic structure should be at least several spatial periods to avoid excessive increases in helicon phase velocity. Finally, the details of the coupling from the helicon waves to the space-charge waves of the drifting electrons have not been considered. The problem is complicated because the fields in the periodic structure of finite width can be represented only by infinite series. For the purposes of the approximate discussion given here, the slow helicons will be represented by the dispersion relation (11), while the space-charge waves of the drifting electrons will be represented by the single line $\omega = qv_0$.

From coupling-of-modes theory one would expect interactions between the slow helicons and the space-charge waves near points where $\omega = qv_0$ intersects $\omega(\beta_0)$ as given by Eq. 11. Consider Fig. XIII-37 which shows a typical plot of Eq. 11. In this plot, the line $\omega = qv_0$ appears as a line of slope $v_0 L\left(\omega_{p1}^2/c^2\omega_c\right)$. Using the parameters from Table XIII-2, this slope is roughly $(7\times10^{-9})v_0 L$, where a minimum magnetic field of 3 kG was assumed to ensure $\omega_c/\nu \gg 1$ as required for low-loss helicon propagation. Since practical limitations on the size of the periodic structure limit L to less than 1 cm, and maximum drift velocities are likely to be of order 10^7 cm/sec, it is obvious that the line representing $\omega = qv_0$ has extremely small slope. For practical purposes

Table XIII-2. Parameters for n-InSb at 77°K.

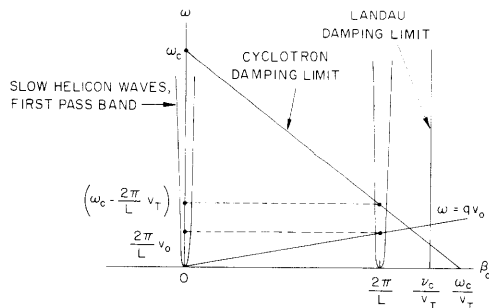|	
Electron Density	$n = 10^{14}$ cm^{-3} (Region I)
Mobility	$\mu = 6 \times 10^5$ cm^2/V-sec
Collision Frequency	$\nu = 1.95 \times 10^{11}$ sec^{-1}
Lattice Dielectric Constant	$\epsilon_L = 16 \epsilon_o$
Electron Effective Mass	$m^* = 0.013 \, m_o$
Plasma Frequency	$\omega_p = 1.15 \times 10^{12}$ sec^{-1}
Cyclotron Frequency	$\omega_c = 1.17 \times 10^{12}$ sec^{-1} per kG
Electron Thermal Velocity at 77°K	$v_T = 5.2 \times 10^7$ cm/sec
Phase Velocity of Light	$c = (\epsilon_L \mu_o)^{-1/2} = 7.5 \times 10^9$ cm/sec

Fig. XIII-39. Simplified picture of slow helicon-space-charge-wave interaction.

the plot can be represented as shown in Fig. XIII-39. Only the lowest passband is of interest, and in this band the line $\omega = qv_o$ lies so low that the helicon waves appear in Fig. XIII-39 as nearly vertical double lines at the locations $\beta_o = 0, \pm \frac{2\pi}{L}, \pm \frac{4\pi}{L} \ldots$.

From Fig. XIII-39, the first interaction appears at a frequency $f_o \approx v_o/L$, which is just the reciprocal of the electron transit time past one spatial period. Other interactions occur near the frequencies nf_o, $n = 1, 2, 3 \ldots$, but these are more likely to lie outside the limits on the solution set by Landau and cyclotron damping. It is interesting to determine requirements for interactions in the range 1 GHz to 10 GHz. Under the assumption of a drift velocity v_o of 2×10^7 cm/sec for the electron stream, which implies an electric field of 33.3 V/cm in the drift region, L must be 2×10^{-3} cm to

produce an interaction at 10 GHz. The corresponding value of β_o, $\beta_o = 2\pi/L = 3.14 \times 10^{+3}$ cm^{-1}, is uncomfortably close to the Landau damping limit $v/v_T = 3.75 \times 10^3$. But, in InSb for temperatures below 77°K, v increases slightly while v_T decreases, so Landau damping could be avoided by using lower operating temperatures. The cyclotron damping limit crosses $\beta_o = 2\pi/L$ at $\omega \approx 3.3 \times 10^{12}$, under the assumption of a magnetic field of 3 kG, so cyclotron damping should not be a problem. In any case, it could be avoided by a sufficient increase in static magnetic field. For operation at 1 GHz with the same drift velocity, a spatial period, 2×10^{-2} cm long, is required. Then, $\beta_o \approx \frac{2\pi}{L} = 3.14 \times 10^2$ cm^{-1}, which is well within the Landau-damping limit at 77°K. As at 10 GHz, cyclotron damping is not a problem.

These preliminary results indicate that an interaction between slow helicon waves and an adjacent drift current is possible at microwave frequencies. Conditions appear somewhat more favorable at 1 GHz than at 10 GHz for structures made of high-purity n-InSb. Several problems remain to be considered, however, before construction of a prototype device could be planned. First, the effects of simple collisional losses on helicon propagation in the periodic structure must be examined. This can be done by retaining the term v/ω_c in Eq. 6 when the dispersion relation for the structure is found. Next, the actual fields in the finite periodic structure and drift region of Fig. XIII-38, and the coupling between the two, should be studied. This may prove to be a difficult problem. One might suspect, however, that shorter spatial periods would lead to weaker fringing fields and consequently weaker interaction in the structure. This suspicion, if correct, would strengthen the earlier conclusion that lower frequencies are favored for obtaining useful interactions. Finally, fabrication of the periodic semiconductor structure itself may be difficult. Individual slabs, 10^{-3} cm thick, would be impossibly fragile, and an increase to 10^{-2} cm would not be a great help. It might be possible, through appropriate control of crystal growth, to form the periodic structure in a single piece of material. This technique would produce a mechanically rugged structure, but might impose an impossible accuracy requirement on the crystal-growing process. These problems merit further study.

R. N. Wallace, A. Bers

References

1. P. Agrain, "Les „Hélicons" dans les Semiconducteurs," Proc. International Conference on Semiconductor Physics, Prague, 1960 (Publishing House of the Czechoslovak Academy of Sciences, Prague, 1961), p. 224.

2. D. A. Watkins, Topics in Electromagnetic Theory (John Wiley and Sons, Inc., New York, 1958).

3. C. R. Legéndy, "Macroscopic Theory of Helicons," Phys. Rev. 135, A1713 (1964).

4. J. Bok and P. Nozieres, "Instabilities of Transverse Waves in a Drifted Plasma," J. Phys. Chem. Solids 24, 709 (1963).

5. G. A. Baraff and S. J. Buchsbaum, "Surface-Wave Instability in Helicon-Wave Propagation," Phys. Rev. 144, 266 (1966).

6. R. N. Wallace and G. A. Baraff, "Surface-Wave Instability in Helicon Propagation. II: Effect of Collisional Losses," J. Appl. Phys. 37, 2937 (1966).